GENERAL INSTRUCTIONS

Team Sizes: 1-4 people
Date of Submitting the Final Report: April 30th 2018; 11:59 pm

No Extensions will be given to this date
You can submit your project report before that day

1. Send an email with your team members, if you are MS or PhD, and the project id
2. When you communicate about your project with us you must send an email to ALL THREE nvtsekos@central.uh.edu, Cristina Morales Mojica <cristina.morales4@upr.edu>
3. **Always start your *email subject* with the Project id.**
4. There will be three project reports: two with the progress of the project and one final
   1st Progress Report: March 24th (25% grade)
   2nd Progress Report: April 7th (25% grade)
   Final Project Report: April 30th (50% grade)

How To

Write your Code: so that one who does not know the subject can follow it!

1. In the beginning of the source code include commends that list all parameters and their defection and explanation
2. Before every loop or if statement etc comment what this is all about
3. use Descriptive names for your parameters or values, e.g. use number_of_interations NOT *N1*!

A report must include:

1. Text report in .DOC (word 2003) organized as: introduction, methods, results, conclusions, references, source code.
2. Source code & Executable
   Important: follow instructions above
3. If used, any input data files
4. Readme file with exact instructions of how you compiles the source, what was your input file
5. A PowerPoint that presents your project organized as (report in (1)
6. An video presentation of the project

How Your Project Will be Evaluated:

1. Based on the readme file, we will compile your code and use the exectutable to run it with your input values (as reported in your readme and in your report0
2. Then we will use another set of input that we know the answer and assess whether your codes produces the same answer
3. If your code does not compile, we will contact you to send us another version in 24hr. If it still does not work, the project is a Fail grade
4. If your code does compile but does not provide the same output with what input you described in your report (i.e. using your inputs) and/or the “known answer input” we use, we will contact you to send us another version in 24hr. If it still does not work, the project is a Fail grade
5. The project report (text, Powerpoint and video) must report in detail
   - Overview of what you did
   - what algorithms you used & what they do
   - how you organized your code
   - what inputs and outputs you got
   - how it performed

Multiple Projects: 2D AND 3D FUNCTION Gradient and Directional Derivative
ID: DERIV2D
ID: DERIV3D

Theme: Learn to extract derivatives and gradients of multidimensional functions, and compare them. Specifically, numerically calculate the directional derivative of a function A and compare it to another function B.

Teams: There are two versions of the project: a 2D for 1 student team and 3D for 2- to 3- student teams. There are other combinations of teams, contact the instructor

Description: Function A in 3D is a function A(x. y, z). First implement the code to calculate the partial derivatives along the three axes (directional derivation) dA/dx, dA/dy and dA/dz. Then calculate the vector d**A**/d**r** (**r** is the unit vector along axis X, Y, Z).

Algorithm Input: function A(x,y)/A(x,y,z), B(x,y)/B(x,y,z), comapriason

Algorithm Output: the derivatives of A(x,y)/A(x,y,z), comparison of the value of derivatives of A(x,y)/A(x,y,z) vs B(x,y)/B(x,y,z) on each axis, comparison of the vector of derivatives A(x,y)/A(x,y,z) vs the vector defined by the B(x,y)/B(x,y,z) function

Provided by the instructor: A(x,y)/A(x,y,z), B(x,y)/B(x,y,z).

Figure below shows an example of how the vectors of the directional derivatives are shown and relate to the function of the ellipses 4x^2+y^2=c, where c is a constant

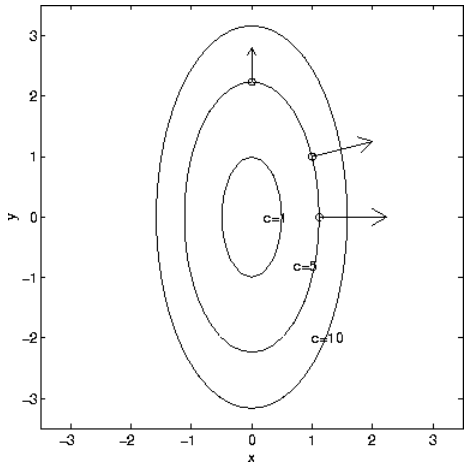

Project : Conservative corridors
ID: ConsCORR

Theme: Implement a numerical approach for 3D segmentation method and generation of rendered 3D and 4D corridors. The segmentation will be based on the Region-Growing algorithm and renderings on meshing. Interpolation will be needed at higher resolution than images requiring careful interpolation so the mesh is concervative in nature and does not collide or cross any structure.

Algorithm Input: Data D(x,y,z), Criterion C(i), Initialization I(x,y,z), k connectivity

Provided by the instructor: Pseudo algorithm of the desired method, Data D(x,y,z), various Criteria C(i), Initialization I(x,y,z,j) and their associated Ground truth GT(x,y,z,i,j,k)

Name	**Explanation**	**Data type/Description**
D	3D data matrix	n x m x k matrix
C	Criterion	Input function
I	Initialization: 3D binary matrix	n x m x k matrix
k	Connectivity parameter	scalar
R	Result: 3D binary matrix	n x m x k matrix
GT	Ground truth: 3D binary matrix	n x m x k matrix

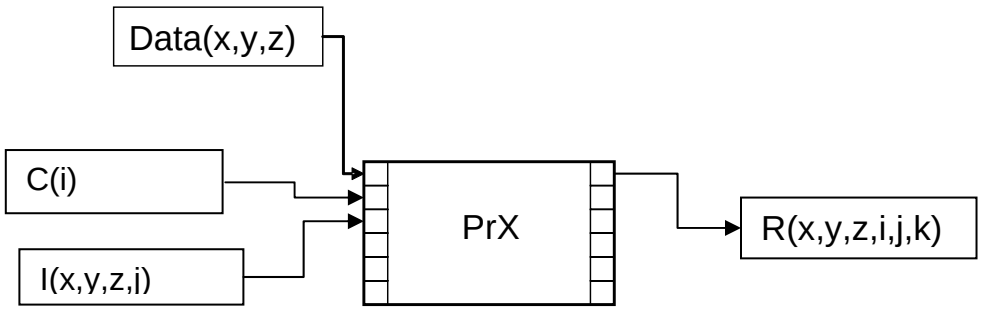

Figure 1: Overview of the code input/output. The output will be compared to GT to test the correctness of the algorithm

Operator Selected Parameters & calculations:

1. *3D matrix:* Input data D and initialization region I.
2. *Function:* Criterion C to apply to grow I using the data D. The function takes as input a set of value and returns an interval of inclusion.
3. *Scalar:* k represents the connectivity of the morphological space and can have 3 values in 3D:
    - *6:* the voxels are considered neighbors if they have one face in common.
    - *18:* the voxels are neighbors if they have at least an edge in common.
    - *26:* the voxels are neighbors if they have at least a vertex in common.

Algorithm Output: The algorithm outputs the final stage R of the growing process as a binary 3D matrix, where the Boolean represents the inclusion or not in the result. This result will be compared to the given ground truth to ensure the process correctness

Algorithms: 3D morphological operations using a customable inclusion criterion

Algorithm pseudo-code:

- Let R_0 be the initial region, i.e. I.
- While R_t is different than R_{t-1} do:
  - Let *t+1* be the current step.
  - Let V be the set of value of the voxels in R_t: V = {D(x,y,z) | R_t(x,y,z) is true}.
  - Let A be the interval resulting of the call C(V).
  - Let $R_{t+1} = R_t$.
  - For each k-connected neighbors (x,y,z) of the voxels in R_t, if D(x,y,z) is included in A, then add (x,y,z) to R_{t+1}.
- Return R, the last iteration of R_t.

Software Output: The software returns a region of k-connected region resulting the growth of an initial region I, using an inclusion criterion C.

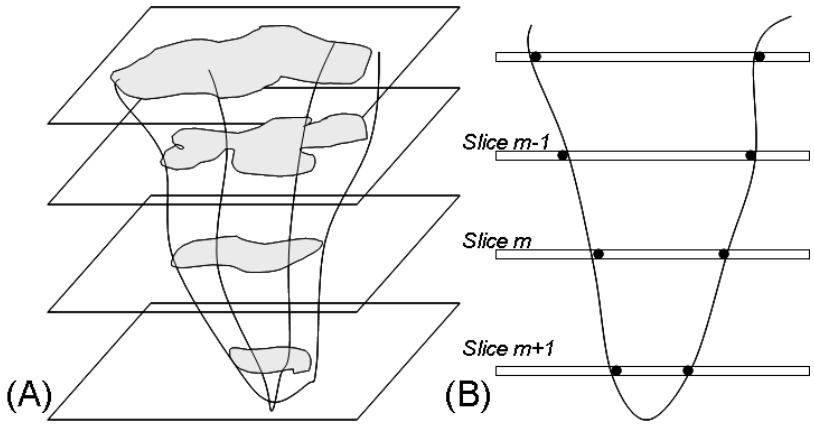

Figure 2: The input will be slices that have a gap between them. After segmentation the segmententation maps will be used to fit a 3D mesh as shown in (A) and (B)

Studies:
Your code will be tested with two data sets provided by the instructor:

1. one will be a CINE MRI set of the beating heart (N slices each capturing the heart motion in M time frames). Thus you will use your algorithm to segment NxM 2D slices. These will then be used to generate a 4D of the segmentation map and a 4D mesh
2. the other will be a set of brain images that will eb sued to extract the vessels and a tumor generating a 3D segmentation map and 3D mesh

All data will provided in DICOM and form the headers you can find their position in 3D space

Spline Interpolation and Error Estimation
id: SPLINE

Theme: implement and study Spline Interpolation of points in 3D

There are several options

See following pages

Cubic Spline Interpolation (CSI)

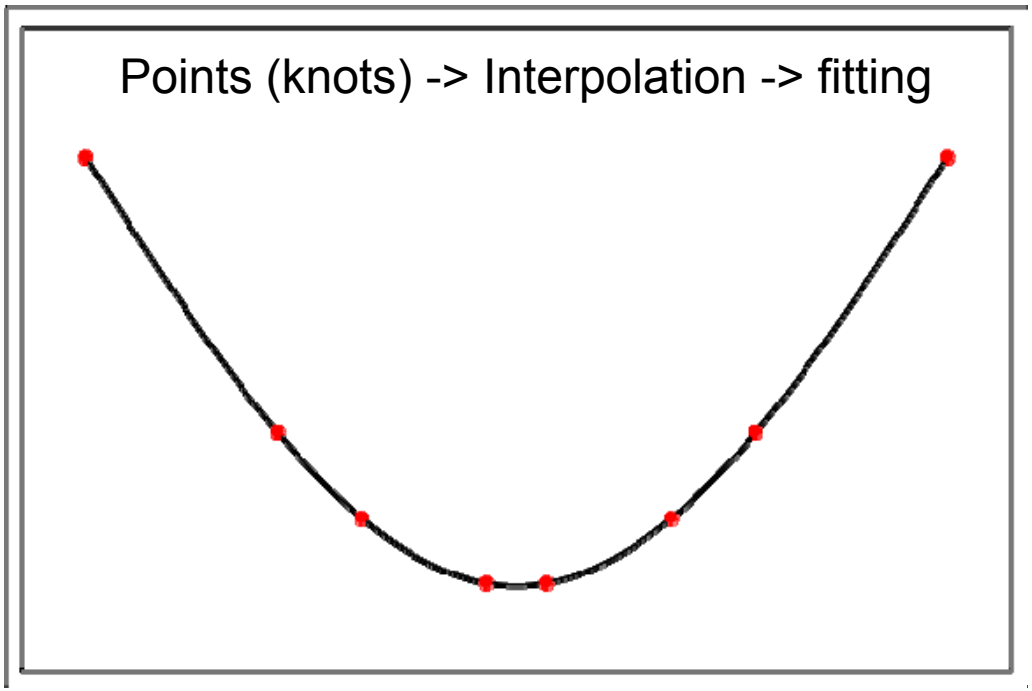

Spline: A numeric function that is defined in a ***piecewise*** manner

- multiple weighted polynomial functions
- smoother transition at knots
- as good as interpolating with high degree polynomials
- immune to instability

Problem Description

Generatea 3D structure when you know portion of it projected in 2D and the 3D coordinates of an ensemble of knots (points)

Assume
a known 3D tubular structure, the prototype structure P(x,y,z)
The ability to get:
1 or 2 projections Pr(J, R, x, y, z) of this shape where J =1 or 2 and R is the plane of the projection
N knots, i.e. Points in space {K(I, x, y, z)} where I = 1, 2, … N

Generate a model of the structure using the Pr(J, R) and the ensemble {K(I, x, y, z)}
-Cubic Spline interpolation function SF(x,y,z)
-Knots {K} and points on the projection Pr(J, R)

Calculate the error SF(x,y,z) vs P(x,y,z)

CSI-1

Find the orientation of the projection plane that optimizes interpolation assuming that you have
1 projection Pr(1, R, x, y, z) and 1 point K(1, x, y, z)
1 projection Pr(1, R, x, y, z) and 2 points K(1, x, y, z), K(2, x, y, z)
1 projection Pr(1, R, x, y, z) and 3 points K(1, x, y, z), K(2, x, y, z) and K(3, x, y, z)

there are certain boundary conditions imposed by
- The Pr(J, R, x, y, z) and {K(I, x, y, z)}
- The length of the structure!!!!

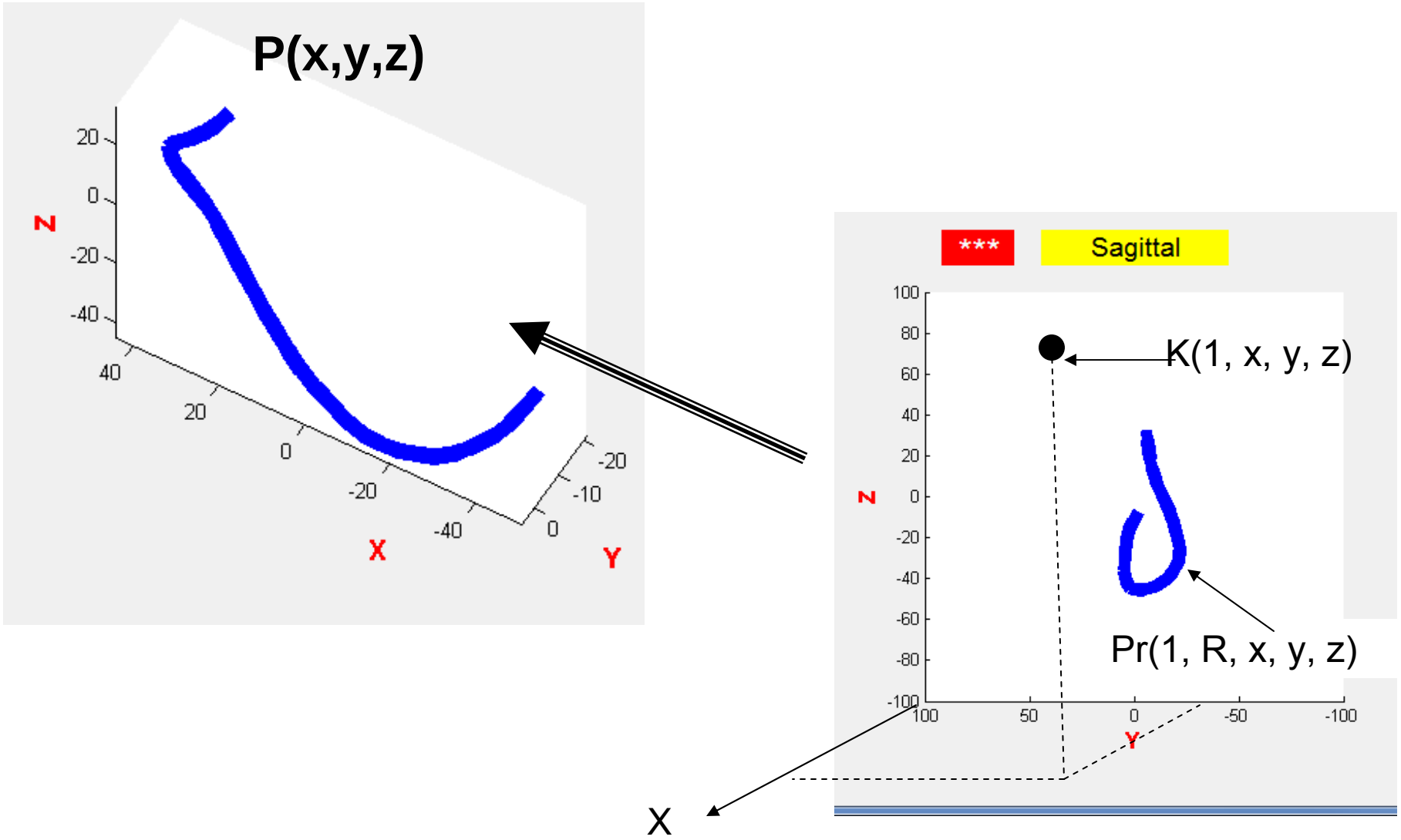
P(x,y,z)
20
0
-20
-40
N
40
20
0
-20
-40
X
-20
-10
0
Y
***
Sagittal
100
80
60
40
20
0
-20
-40
-60
-80
-100
N
K(1, x, y, z)
Pr(1, R, x, y, z)
100
50
0
-50
-100
Y
X

CSI-2

In this case, assume that you have an ensemble of points (K(J, x, y, z)) and you know the projection of *a segment* of the the projection i.e. NOT the projection of the entire length! Then

Find the minimum number of (K(J, x, y, z)) knots that are needed to generate the original structure for different known segments

Generate a “moving window” on the structure and use the transient 2D projection of this window and 3D knots to generate the structure

Length of moving Window (independent of shape)
Number of knots
Length of P(x,y,z)

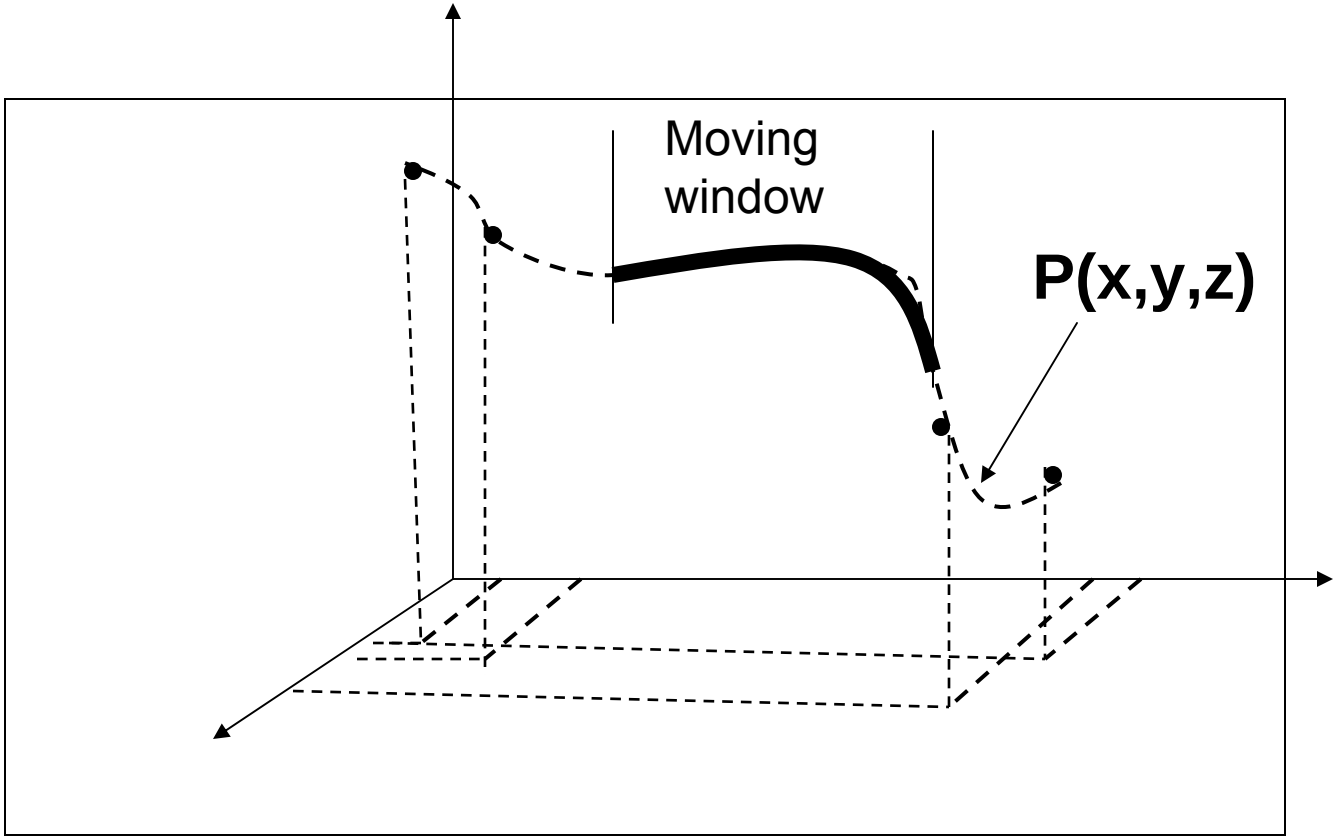

Interpolation Issues: Runge

This family of project will deal with Runge phenomenon that pertains to the interpolation of equally spaced points and the errors secondary to this type of distribution.

This is a very imporant phenomenon with consequences in sampling real data!

- Analyze the reasons for this phenomenon
- Relate to the Gibbs phenomenon (and Gibbs artifacts)
- Then, compare the equally spaced to Chebyshev points

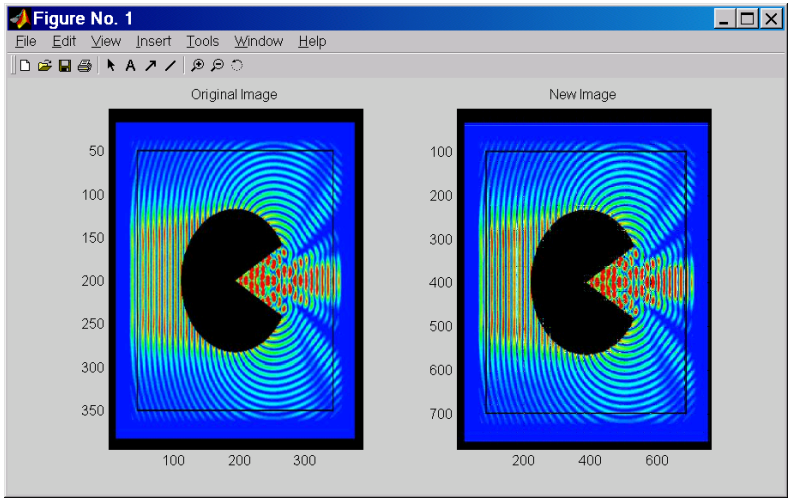

Runge Phenomenon (Oscillations)

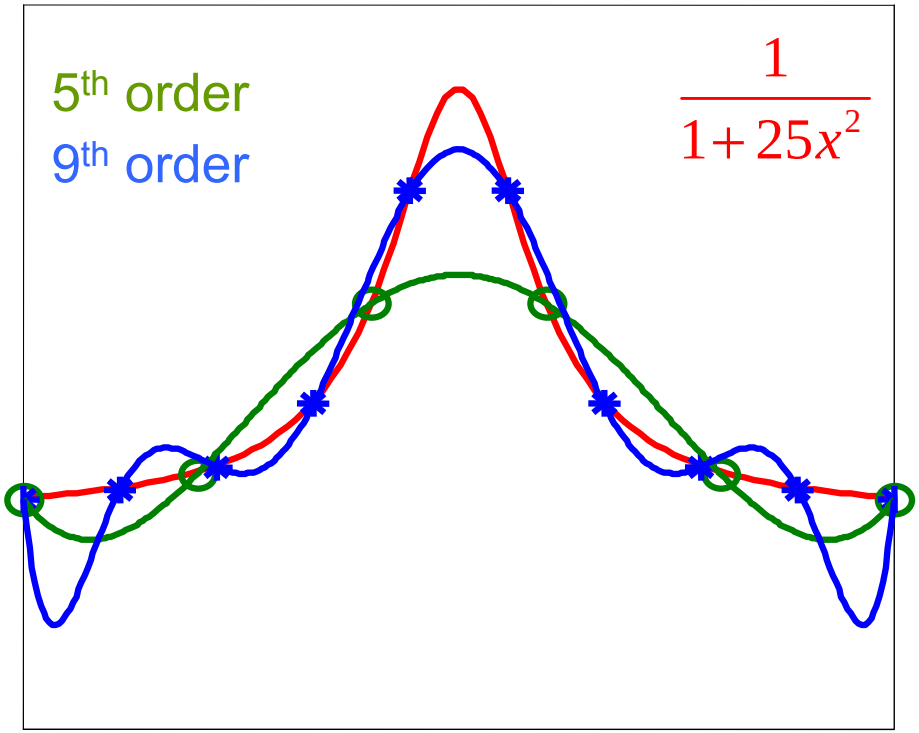

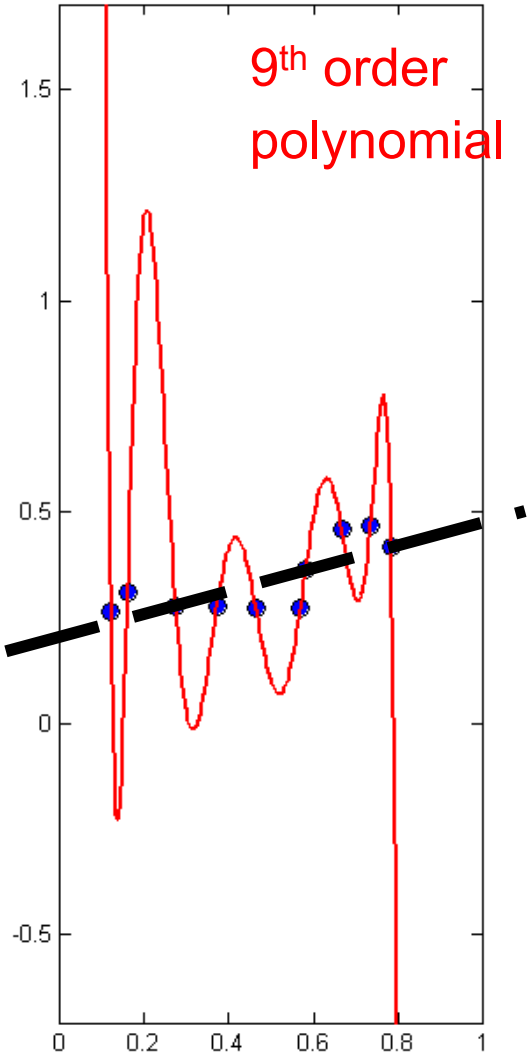

- What is practically a good polynomial order?

This is a report on splines

You can use this as a starting point for your work

Contents

1 Introduction

Interpolation

In most of the scientific applications we only know a limited number of data which represent the values of a function for a limited number of values of the independent variable. So whenever we want to know the values at some unknown points we always need to estimate the values of the function for some intermediate values of the independent variable. This can be achieved using Curve fitting.

This can be done using various methods like

1. Piecewise constant interpolation
2. Linear interpolation
3. Polynomial interpolation
4. Spline interpolation.

B-Spline Interpolation

B-Splines find their applications in the construction of Rail Road Tracks, ships and flights etc. In flight modeling and production, splines can be used to represent machine tool cutter paths, engineering analysis and simulation, navigation and guidance systems. For instance, we consider the navigation systems, the entire path of the flight needs to be generated from a given set of locations (which can be considered as "Control Points") on the globe. Given the source and destination locations, we need to generate a smooth plan that passes through the first and last control points, which is where we bring the B-Splines into the scenario. The objective of this project is to generate a smooth spline using the given set of control points.

Advantages of choosing this method over the other methods

B-Spline interpolation is very useful when compared to other parametric curves because in case of other curves the order of the curve is fixed based on the number of control points so as the number of control points increases the order of the curve increases which makes it complicated to perform calculations. B-Spline curves overcome this disadvantage.

For example if we are taking 4 control points then the degree of the polynomial that we need to solve would be 4 and as we increase the number of control points this degree increases making it more complicated. But using B-Spline curves we can even control the degree of the polynomial that need to be generated.

Moreover B-Spline curves also has the advantage of local propagation unlike global propagation of other methods. In other interpolation methods as it is a global propagation if there is a change in a single control point the shape of the complete interpolant changes but in the case of B-Spline even though there is a change in a single control point it only changes the segments which are related to this control point and all other segments are not affected.

2 Process

The major steps involved in the Spline Fitting and Error Estimation are as mentioned below:

1. Generating the Knot vector
2. Implementing the Deboor's Algorithm for B-Spline Interpolation
3. Sampling the points, to test the B-Spline Interpolation
4. Estimating the error between the original and test splines

Approach

The spline fitting involves capturing the user input which are referred to as Control points P_i, then generating the Knot Vector t based on the order, k of the piecewise segment of the B-Spline and the number of points, n. The knot vector is then used to interpolate the user input by solving the Deboor's recurrence formula r. The output of the interpolation gives a set of points (which we term as "Ground truth") stretched between the first point and the last point, which are smoothed by the control points. The order k determines how many control points effect each segment in the B-Spline. By default, we have taken the value of k to be 3, since it solves global propagation problem compared to other interpolation methods and maintains curvature continuity, meaning that two curves joining at a point they go in the same direction where they meet and also have same radius at that point and also slope continuity, meaning that the two curves not only touch, but they do even go in the same direction at the point where they touch.

3 B-Spline Interpolation

Given a set of points and the order of the segment, the first and last points control only one segment within the B-Spline. Remaining points control the segments depending upon the value of k.

3.1 Knot Vector Generation

Once we obtain the n+1 control points P_0, P_1, P_2,....., P_n and degree k, we can generate a knot vector. For a B-Spline curve of degree k, we need m+1 knots where m=n+k+1. Precisely, the first k knots are 0's and the remaining knots would be in an incrementing order till the $(m-k)^{th}$ knot and the last k knots will have the same value.

$$t_i = \begin{cases} 0 & if\ i \leq k \\ i-k & if\ k \leq i \leq n \\ n-k+2 & if\ i > n \end{cases}$$

3.2 Deboor's Algorithm

B-Spline can be simply defined as a composite curve which consists of various number of curves. The degree of a B-Spline curve can be independent of the number of control points. B-Splines maintain local control, hence any change in one of the control points doesn't change the entire curve but only the segments which depend upon that particular control point. While there are many spline interpolation techniques, we have used the Deboor's algorithm for fitting the spline. According to the algorithm, a B-Spline curve can be defined as a linear combination of control points P_i and B-Spline basis functions $N_{i,k}(t)$ given by:

$$r(t) = \sum_{i=0}^{n} p_i N_{i,k}(t), \qquad n \geq k-1,\ \ t \in [t_{k-1}, t_{n+1}]$$

Where k is the order of each of the piecewise polynomial segments that form the B-Spline curve. A polynomial of degree 3 solves the problem of slope continuity and curvature continuity, hence in our project we choose the k value to be 3. A polynomial degree above 3, doesn't have any signification change. The basis function for the B-Spline is defined by the Knot-Sequence t. The basis function for a polynomial segment of the order of k can be defined as below:

$$N_{i,1}(t) = \begin{cases} 1, & if\ t \in [t_i, t_{i+1}), \\ 0, & Otherwise \end{cases}$$

and if $k > 1$,

$$N_{i,k}(t) = \left(\frac{t - t_i}{t_{i+k-1} - t_i}\right) N_{i,k-1}(t) + \left(\frac{t_{i+k} - t}{t_{i+k} - t_{i+1}}\right) N_{i+1,k-1}(t)$$

Where t defines the Knot vector. By solving the equation $r(t)$, we generate the data points Di which form the spline and are controlled by the control points Pi.

4 Sampling Points

After generating the "Ground Truth" i.e., the data points D_i, we do sampling to select n control points to generate a new spline. These new set of control points will be referred to as S_i. We have used three different samples to analyze the performance of the interpolation method we have implemented:

4.1 Left-Skewed: Choosing the control points such that, more points towards the beginning of the curve and fewer points towards the ending of the curve.

4.2 Right-Skewed: Choosing the control points such that, fewer points towards the beginning of the curve and more points towards the ending of the curve.

4.3 Uniformly-Distributed: Choosing the control points such that they are uniformly distributed from the beginning to the ending of the curve.

5 Error Estimation

Once we have the test set of control points S_i, we interpolate the sample using the knot vector and deboor's algorithm for spline interpolation. The interpolated points are then plotted. The plot clearly shows the deviation of the test samples from the "Ground Truth". We then calculate the average error distance between the original and the test sample curves. We have used Euclidean distance between each of the points. The average of the sum of all the distances gives the amount of deviation. We calculate the error using the below mentioned formula:

$$dist\big((x_1, y_1, z_1), (x_2, y_2, z_2)\big) = \sqrt{(x_1 - x_2)^2 + (y_1 - y_2)^2 + (z_1 - z_2)^2}$$

Average of the Error distance:

$$\frac{dist\big((x_1,y_1,z_1),(x_2,y_2,z_2)\big)}{n},$$

Where n is the number of points in "Ground Truth" D_i

6 Tools

We have implemented the project in MATLAB. It provides a variety of tool bars which enable for a better GUI and proper plotting in 3-D Co-ordinate system.

7 Algorithm

The spline fitting and error-estimation consists of the following steps:

i. Input a set of 'n' points and order 'k' for the piecewise polynomial
ii. Calculate the Knot Vector
iii. Generate the piecewise polynomial equation for each of the segments between two control points using Deboor's algorithm
iv. Generate the spline from the output set of points from spline interpolation
v. Select a set of points from the spline satisfying the following three conditions:
    - Points sparse towards the beginning of the spline curve
    - Points sparse towards the end of the spline curve
    - Points equally distributed throughout the spline
vi. Interpolate the BSpline
vii. Estimate the error

Block Diagram:

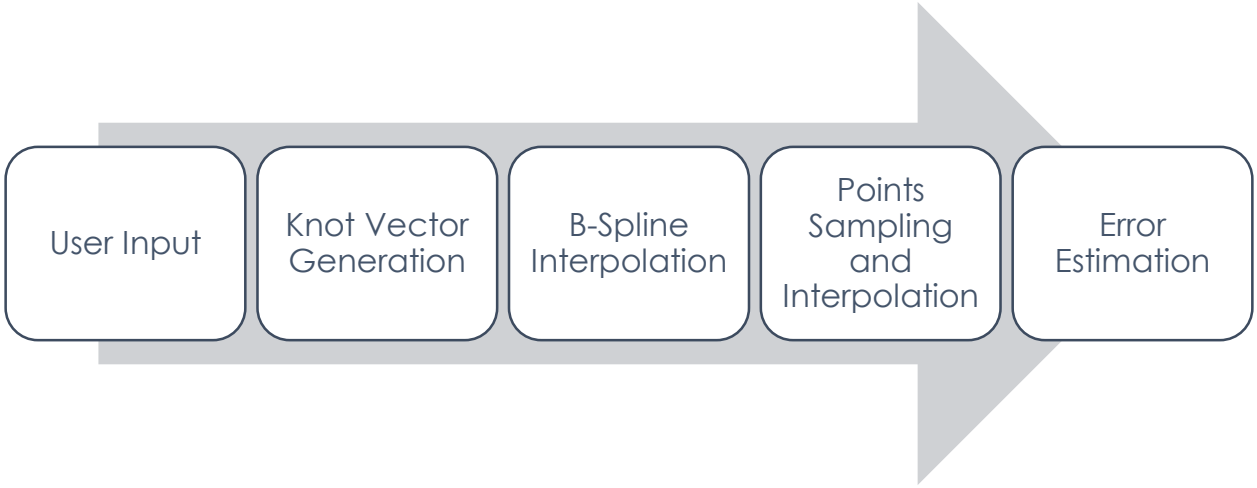

8 Experiments and Results

8.1 Capturing Input Data Points

Our implementation provides with two options to enter the input points:

- Manual
- GUI

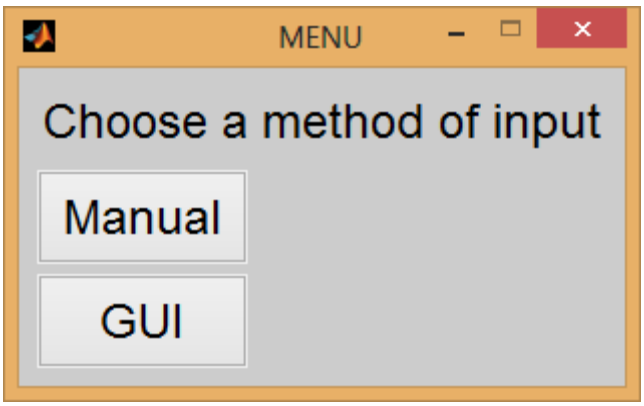

Fig 1: Choosing the method of input

8.1.1 Manual Input

For manual input of points we display a textbox to insert the co-ordinates by separating with commas. Ex: 1.45, 2.35, 3.45

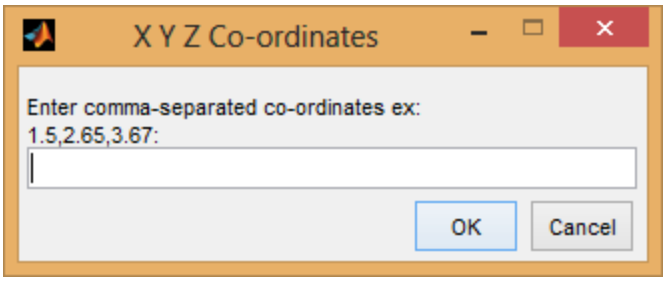

Fig 2: Manual method of input

8.1.2 GUI

For selecting the input points through GUI, we first display an empty X-Y axis and select the x, y co-ordinates. Then in another plot we display the Y-Z axis and restrict the selection of z, to only the corresponding y, z co-ordinates where y is from the previous selection. Once you select a point in Y-Z plot, user should press enter to confirm the selection. The below images show the two axes which are used for the selection of x, y and z co-ordinates:

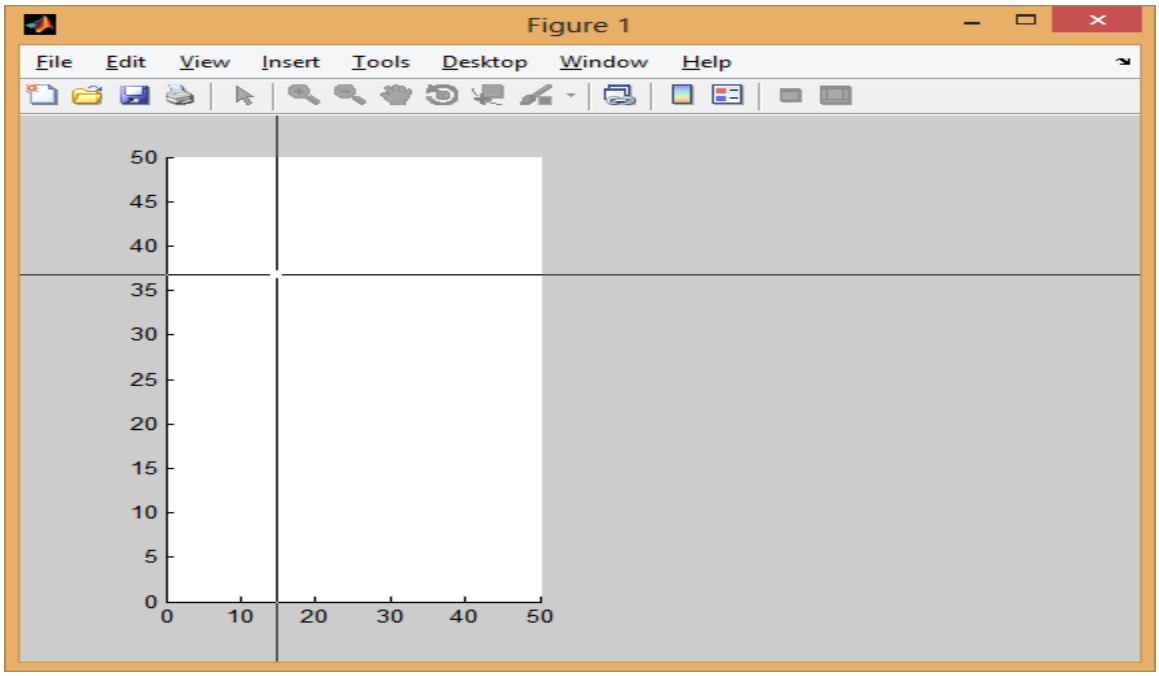

Fig 3: Capturing the x, y co-ordinates

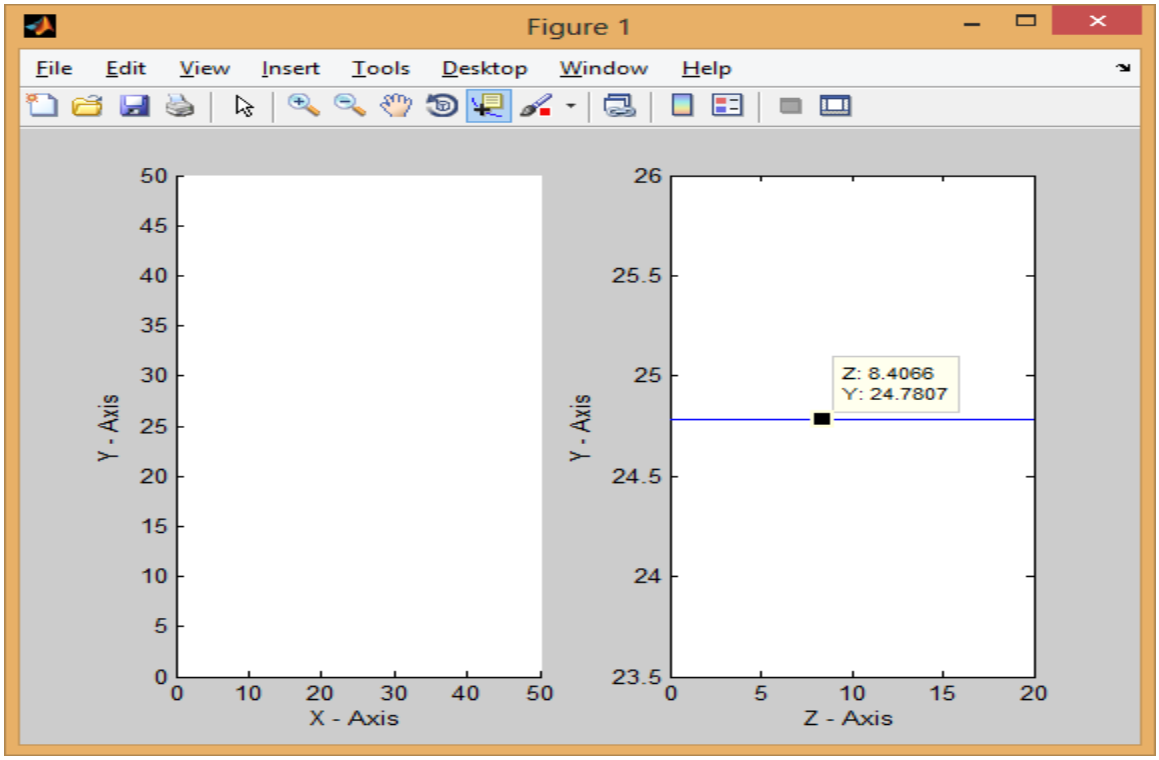

Fig 4: Capturing the y, z co-ordinates

8.2 Testing the method with various Data Points

We have tested the Spline interpolation with various points and estimated the error generated for three data samples. Given below are various datasets and the corresponding spline plots.

8.2.1 Input Data 1

X	6.01	18.58	15.64	42.11	65.90	68.85
Y	36.62	25.65	15.27	19.66	17.61	10.89
Z	15.47	18.35	32.07	41.32	40.37	48.35

The output obtained by interpolating the above points is shown in the figure below:

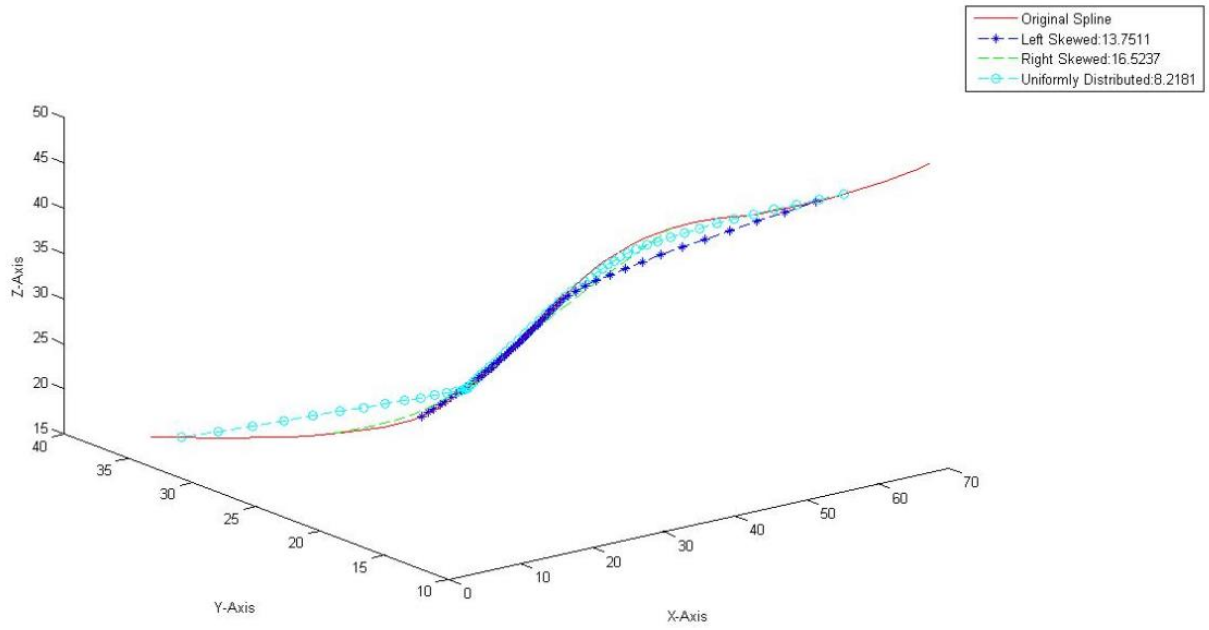

Fig 5: Plot of the original spline and Sample Test Splines

The above image displays the original alpine and the test splines generated from sampling the "Ground Truth". The top-right corner of the image displays various line formats used for each of the splines and also the corresponding average error distance for the Left-Skewed, Right-Skewed and Uniformly Distributed samples.

8.2.2 Input Data 2

X	6.81	17.78	36.22	40.50	60.56	96.65
Y	20.24	31.50	24.92	11.76	31.06	29.60
Z	2.2447	3.67	6.32	3.244	7.39	14.09

The output obtained by interpolating the above points is shown in the figure below:

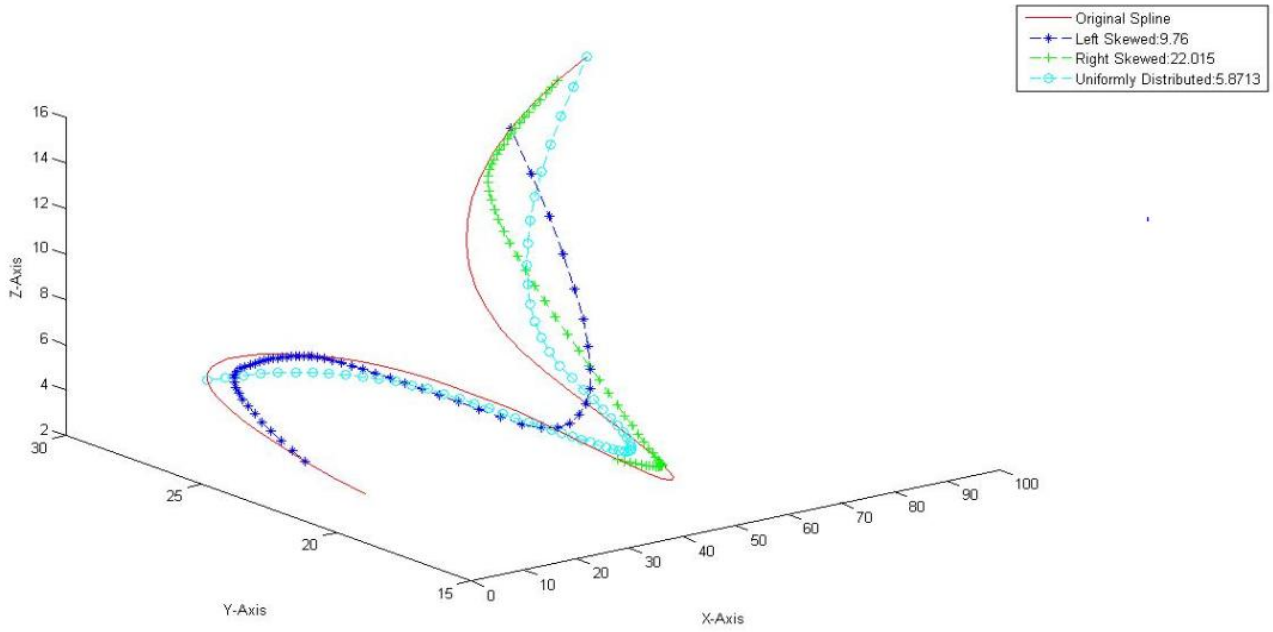

Fig 6: Plot of the original spline and Sample Test Splines

The above image displays the original alpine and the test splines generated from sampling the "Ground Truth". The top-right corner of the image displays various line formats used for each of the splines and also the corresponding average error distance for the Left-Skewed, Right-Skewed and Uniformly Distributed samples.

8.2.3 Input Data 3

X	18.85	27.40	47.727	65.64	91.31	120.187
Y	27.41	17.90	34.137	34.42	15.277	30.92
Z	6.428	5.769	11.923	14.011	18.73	18.406

The output obtained by interpolating the above points is shown in the figure below:

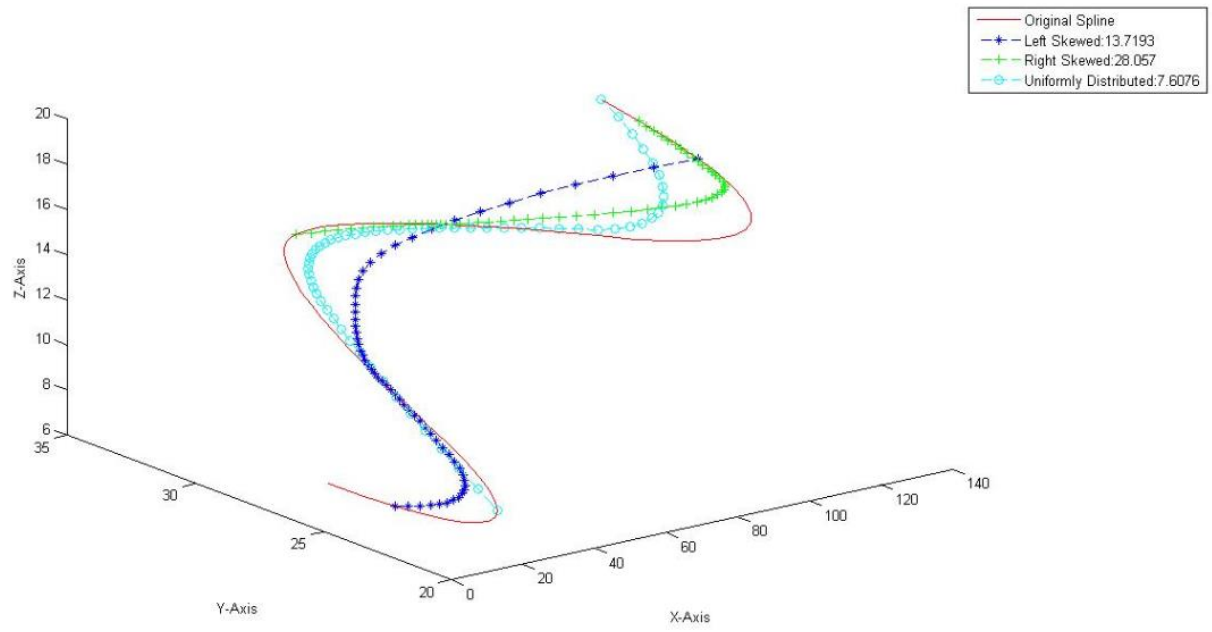

Fig 7: Plot of the original spline and Sample Test Splines

The above image displays the original alpine and the test splines generated from sampling the "Ground Truth". The top-right corner of the image displays various line formats used for each of the splines and also the corresponding average error distance for the Left-Skewed, Right-Skewed and Uniformly Distributed samples.

8.3 Observations

From the above tests the following observations have been made regarding the average error distance:

	Dataset 1	Dataset 2	Dataset 3
Left-Skewed	13.7511	9.76	13.7193
Right-Skewed	16.5237	22.015	28.057
Uniformly-Distributed	8.2181	5.8713	7.607

The above table displays the corresponding average error distances calculated for the test samples, generated from each of the datasets. From the above table, following observations can be made:

- The average error distance is less for the uniformly-distributed test sample in all of the datasets.
- The average error distance for left-skewed and right-skewed test samples doesn't follow any specific trend.

9 Challenges

Initially when we started with getting input from the user using a GUI we faced issue with getting a 3D input from the user because so we finally decided with getting the 3D input in two 2D planes like XY plane and YZ plane. For this first we are asking user to select a point from the XY plane and once he selects a point as we know the Y coordinates, in the YZ plane we are restricting the user to this Y value and asking him to select some Z value.

10 Conclusions

From the above experimentations we can conclude that the number of points and the distribution of these points affects the shape of the B-Spline generated.

11 References

https://www.wikiwand.com/en/Interpolation
https://www.wikiwand.com/en/B-spline
http://www.geos.ed.ac.uk/~yliu23/docs/lect_spline.pdf
http://scholar.lib.vt.edu/theses/available/etd-04192001-172731/unrestricted/chapter_4.pdf

Function Filters
id: FILTER

Theme: implement and study algorithms for processing digital images

Study the included paper and implement Frangi filter

The Original work of Frangi Filter is this:
http://www.tecn.upf.es/~afrangi/articles/miccai1998.pdf

2017 IEEE/RSJ International Conference on Intelligent Robots and Systems (IROS)
September 24–28, 2017, Vancouver, BC, Canada

Towards MRI-Guided and Actuated Tetherless Milli-Robots: Preoperative Planning and Modeling of Control

Thibault Kensicher*, Julien Leclerc*, Daniel Biediger, Dipan J. Shah,
Ioannis Seimenis, Aaron T. Becker, Nikolaos V. Tsekos

***Abstract*— Image-guided and robot-assisted surgical procedures are rapidly evolving due to their potential to improve patient management and cost effectiveness. Magnetic Resonance Imaging (MRI) is used for pre-operative planning and is also investigated for real-time intra-operative guidance. A new type of technology is emerging that uses the magnetic field gradients of the MR scanner to maneuver ferromagnetic agents for local delivery of therapeutics. With this approach, MRI is both a sensor and forms a closed-loop controlled entity that behaves as a robot (we refer to them as MRbots). The objective of this paper is to introduce a computational framework for preoperative planning using MRI and modeling of MRbot maneuvering inside tortuous blood vessels. This platform generates a virtual corridor that represents a safety zone inside the vessel that is then used to access the safety of the MRbot maneuvering. In addition, to improve safety we introduce a control that sets speed based on the local curvature of the vessel. The functionality of the framework was then tested on a realistic operational scenario of accessing a neurological lesion, a meningioma. This virtual case study demonstrated the functionality and potential of MRbots as well as revealed two primary challenges: real-time MRI (during propulsion) and the need of very strong gradients for maneuvering small MRbots inside narrow cerebral vessels. Our ongoing research focuses on further developing the computational core, MR tracking methods, and on-line interfacing to the MR scanner.**

I. INTRODUCTION

Minimally invasive procedures with real-time image guidance are being established in the clinical realm. An ever-growing body of literature supports the potential of magnetic resonance targeting (MRT) to maneuver tiny tetherless therapeutic entities inside natural body pathways (such as vessels) to a targeted pathologic locus. MRT offer unparalleled potential to improve patient outcome. It is based on using the magnetic field gradients of an MRI scanner, used for signal spatial encoding and image generation, to propel and accurately maneuver a ferromagnetic object [1]–[3]. The fundamental benefit of MRT is its tetherless nature: no catheters, guidewires or other mechanical support that can harm tissue is needed; this is of paramount importance especially for paths inside small vessels (brain arteries) or quickly moving vessels (coronary arteries). The potential success of MRT can be transformative and eventually a paradigm shift for a plethora of interventions. This argument is eloquently stated by Sitti et al, [4] "One of the highest potential scientific and societal impacts of small-scale (millimeter and submillimeter size) untethered mobile robots would be their healthcare and bioengineering applications". An MRT system can be envisioned as operating in a closed loop fashion using the MR scanner (i.e. its gradients and data acquisition) in this dual role to propel and track these entities. This system behaves and can be described as a robotic system. A version of such system may entail the propulsion and maneuvering of an assembly of such entities; in this case we have a unique paradigm of robotic swarms driven by a single source [5]. Another case is when a single ferromagnetic entity, such as a sphere, is propelled and maneuvered inside the human body. In this article we will focus on that case and for simplicity we will refer to them as MRbots. An MRbot controller must know the position of the object and the roadmap. A ferromagnetic object produces a large artifact that can then be used to track the object by rapidly collecting, for example, signal intensity projections along the three axes of the gradients

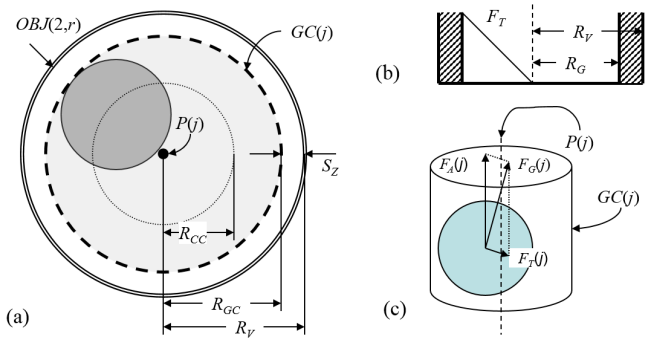

Fig. 1. MR-based servoing of the MRbots (a) From the segmented vessel $OBJ(2,r)$ are extracted the Path $P(j)$ and the virtual guidance corridor $GC(j)$ (dashed circle) is generated with a safety zone S_Z. (b) The $GC(j)$ imposes a forbidden boundary behind which the MRbot should not reside. (c) The gradient exert force $F_G(j)$ analyzed in two components, a propulsion $F_A(j)$ and a correction transverse $F_T(j)$.

(*) equal contribution

This work was supported by the National Science Foundation under Grant No. [CNS-1646566]. NVT and IS acknowledge in part support by the Stavros Niarchos Foundation that is administered by the Institute of International Education (IIE). All opinions, findings, conclusions or recommendations expressed in this work are those of the authors and do not necessarily reflect the views of our sponsors.

T. Kensicher, D. Biediger, and N. Tsekos are with the Dept. of Computer Science, University of Houston, Houston, TX 70004, USA nvtsekos@uh.edu

J. Leclerc and A. Becker are with the Dept. of Electrical and Computer Engineering, University of Houston, Houston, TX 70004, USA jleclerc@uh.edu; atbecker@uh.edu

D. Shah is with the Cardiovascular Imaging Institute, Houston Methodist DeBakey Heart & Vascular Center, Houston, TX 77030, USA

I. Seimenis is with the School of Medicine, Democritus University of Thrace, Alexandroupolis, Greece iseimen@med.duth.gr

[6]. When the anatomical structure is rather static, such as the brain vasculature, then the roadmap can be generated from preoperative high resolution multislice or 3D MRI, such as magnetic resonance angiography. While continuous on-the-fly imaging and propulsion is preferable, with boluses of ferromagnetic entities, imaging can be interleaved with propulsion in an open-loop control scheme. In this case, after a propulsion step, imaging can be collected and for the next step of propulsion, the gradients are adjusted to maneuver the bolus using the predefined roadmap of the vasculature [7].

Among the clinical paradigms that may have the potential to highly benefit from this robotic technology are interventions into tortuous vessels and moving anatomies, such as the heart and the coronary arteries. To ensure safety and accuracy, such procedures require continuous on-the-fly imaging (to both track the MRbots and image the pathway) and propulsion. For the purpose of MRbot control, this challenge can be appreciated considering that even a high resolution MRI, e.g. pixel sizes 0.25 to 0.5 mm, may not be sufficient to accurately image a 1-2 mm diameter vessel; this is highly demanding considering that in vivo the vessel is a 4D structure. In the absence of propulsion, practical real- time MRI (rtMRI) can be achieved even with multislice MRI as was shown in cardiovascular procedures [8], [9]. The challenge is that with MRbots the gradients are also used for propulsion and there is a priority conflict: one needs to safety maneuver, which in turn requires continuous MRbot tracking and path imaging. Alternative approaches need to be considered paving the way toward such in vivo interventions.

Prior groundbreaking works in vivo and in vitro have controlled the MRbots along a path between waypoints, for example [7]. Recently a study described a fast method to combine the propulsion and tracking [6]; still we are lacking intraoperative path imaging and the need to follow a trajectory without knowledge of consequences of an error. A method complimentary to trajectory planning, which requires accurately following a well predefined path to ensure safety, is to control the MRbot to maneuver inside the tubular corridor defined by the vessel itself. Maneuvering inside a corridor that is narrower than the vessel offers a margin of error without colliding or perforating the vessel wall. This concept has been explored before in catheter-based vascular and cardiac interventions introducing virtual fixtures (VF), i.e. imaging-based software-generated virtual constraints, for improving safety and accuracy of telemanipulation systems [8]–[12]. Such an approach can address the limited spatial resolution of preoperative and intraoperative MRI as shown before in cardiac interventions [8], [9], [12]. From the large number of pioneering works in VF robot guidance, we review a small pertinent sample. Howe et al. first introduced the innovative concept of VF for cardiac surgeries (coronary artery bypass graft procedures) using computed tomography (CT) images [10]. An important contribution was by Ren et al. that introduced the concept of dynamic virtual fixtures, generated by creating a visual/haptic model from preoperative dynamic MR/CT images and registering it using intraoperative ultrasound images, for minimally invasive robot assisted cardiac surgeries [11]. Yeniaras et al. described the generation of dynamic deformable volumes inside the left ventricle of the heart for safe access to the aortic root using pre-operative and single slice rtMRI [12]. Navkar et al. introduced the use of multislice rtMRI to update a 4D virtual corridor on-the-fly [9] and force-feedback interactive control [13] for intracardiac surgeries, that was then combined into an integrated framework for rtMRI/VF-based robot control [14]. These, as well as other works in medicine or other control domains, demonstrated the value of virtual cues generated from imaging to guide a manual or robotic procedure.

This work is a first step toward buiding a system for performing tetherless MRbot interventions from the MRI servoing perspective. It focuses on implementing a prototype computational framework for MRI/VF-based visual-servoing of tetherless MRbots. It introduces the use of VF, extracted from pre-operative multi-contrast MRI, to generate virtual guidance cues for maneuvering MRbots inside tortuous vessels: 1) a guidance path along the centerline of the vessel which acts as the preferred trajectory, and 2) a virtual guidance corridor that follows the guidance path with diameter adjusted to be smaller than the vessel diameter locally (within which the MRbot can safely maneuver, see Fig. 1). The guidance cues are then used by (1) the gradient generation module to calculate the needed magnetic force exerted onto the MRbot and generate the corresponding gradient waveforms and (2) the closed-loop speed and position controller. Those cues are in a format ready to provide visual cues to the operator via a display or augmented reality devices. Since on-line access to an MRI scanner was not available, this prototype framework was tested in silico, simulating the maneuvering of a sphere from an entrance location to a targeted lesion for the clinical paradigm of brain meningioma. Section II describes the implemented framework, Section III describes and presents results from the in silico studies, Section IV discusses the system and its limitations, and Section V concludes and discusses future works.

II. Methods

A. Overview of the VF Approach

In a typical scenario of a procedure performed via a vascular access, a tetherless MRbot is introduced into the vessel at an inlet location *In*, as example via an intravascular (IV) cannulation, and maneuvered toward a targeted location T. Generation of the guidance cues is based on assuring that the MRbot (1) does not harm the vessel (e.g. perforation or rubbing), and (2) accurately reaches the targeted anatomy. In this work we made two assumptions. First, all structures are static; this is appropriate as a first approximation to describe the vascular tree in the clinical paradigm of interventions in the brain. However, this is not the case in other organs, for example in the coronary arteries or in the heart blood chambers in which cases the guidance cues are dynamic (for example as shown before in [9], [12]). Second, the MRbot size is such that it can maneuver inside the entire length of

TABLE I
DATA USED BY THE COMPUTATIONAL CORE.

Entity	Description	Source	Used by	file
$MR(c)$	MR data	MRI	PIPm, VISm	.dcm
In, T	Inlet and Target	PIPm	PLm	(*)
$OBJ(1,r)$	Segmented tumor	PIPm	VISm	.jpg
$OBJ(2,j)$	Segmented blood vessels	PIPm	VISm	.jpg
$OBJ(3,j)$	Segmented skin 1	PIPm	VISm	.jpg
$OBJ(4,j)$	Segmented skin 2	PIPm	VISm	.jpg
$P(j)$	Path	PLm	CNRm VISm	(*)
$GC(j)$	Guidance corridor	PLm	CNRm, VISm	.srt
$\kappa(j)$	Curvature	PLm	CNRm	(*)
$V(j)$	Velocity profile	PLm	CNRm VISm	(*)
$G(r,t)$	Gradient waveform	CNRm	MRI	.cpp

PIPm: Preoperative Imaging Processing module;
PLm: Planner module;
CNRm: control module;
VISm: visualization module;
(*) elements of the matrix.

the vessel of interest; in practice spherical MRbots can be produced in different sizes (that does have consequences as discussed in Section III-B).

Figures 1(a)-1(b) illustrate the proposed approach. The magnetic resonance angiography (MRA) is segmented to generate the vascular tree $OBJ(1,j)$. The index j refers to the digitized form of the MRA 3D vascular path. The centerline $P(j)$ and a guidance corridor $GC(j)$ are generated so that the radius $R_{GC}(j)$ of the $GC(j)$ is smaller than the diameter $R_V(j)$ of the segmented structure $OBJ(1,j)$. An MRbot can safely maneuver in the 3D cylinder with radius $R_{GC}(j)$ surrounded by a ring-like safety zone $S_Z(j) = R_V(j) - R_{GC}(j)$ within which no motion is allowed. The operation of this control scheme can be appreciated considering that the force $F_G(j)$ applied to the MRbot at location j has a "forward" propulsion F_A and a transverse correction component F_T; that are synchronously adjusted to keep the MRbot always inside $GC(j)$ and as close to $P(j)$ as possible.

B. Computational Framework

In the computational core the 3D vascular path is represented as a (6, N_P) matrix where N_P is the digitization number after processing the MRA data. 3 coordinates $[X(j), Y(j), Z(j)]$ of the centerline point, the radius of the vessels $R_V(j)$, the radius of the guidance corridor $R_{GC}(j)$, and the curvature $\kappa(j)$; i.e. as illustrated in Fig. 2(a) the path is visualized as a linear entitiy $[X(j), Y(j), Z(j), R_V(j), R_{GC}(j), \kappa(j)]; 1 \leq j \leq N_P$. In the prototype version, the computational core is composed of four task-dedicated software modules, as illustrated in Fig. 2. Parameters of the routines are accessible via the graphic tools of the GUI shown on the LCD and/or of a HoloLens. Table 1 reviews the parameters for ease of reference. The core was developed and tested on MATLAB for flexibility in testing image-based processes; but MATLAB does not offer the benefits of C/C++ and associated libraries.

C. Preoperative Imaging Processing Module (PIPm)

The input to the PIPm are the preoperative MRI data that are processed to render the anatomical structures of interest that will then be used by the Planner and the Visualization modules. Currently, the PIP module includes three routines for segmentation of the tumor, the skin and vessels.

Extraction of Tumor: The tumor, $OBJ(1,r)$, was extracted from the multislice set of Post-Contrast T1-weighted Fast Field Echo (post-T1FFE). A region-growing algorithm was manually seeded by creating a few polygons inside the tumor. The tumor was then segmented based on the criterion introduced by Pohle et al. in [15]: at step t, all voxels connected to the existing region $R(t-1)$ are added to $R(t)$ if their value is included in $I(t)$ where:

$$I(t) = [v - \alpha \cdot \sigma^-; v - \alpha \cdot \sigma^+] \quad (1)$$

with v being the median of all the values of the voxels included in $R(t-1)$, α a user-selected parameter set visually, σ^+ the standard deviation of the values of $R(t-1)$ that are greater than v and σ^- the standard deviation of the values of $R(t-1)$ that are lower than V. Two voxels are connected if they have at least one vertex in common.

Upon completion of the region growth step, the surface is smoothed using a morphological closing with a sphere mask to erase small gaps due to noise. In our case, an α of 1.5 allowed us to segment the tumor.

Extraction of Blood Vessels: Arteries $OBJ(2,r)$ were extracted from the multislice set of Time Of Flight (TOF) magnetic resonance angiography (MRA). Segmentation was based on a simple signal intensity high-pass filtering algorithm, i.e. thresholding. Two combined manual thresholds were used: the first was directly applied on the value of the voxels, while the second used the results of a Frangi filter to allow finer vessels to appear [15]. The filter allows the user to be less restrictive when applying the threshold on the value of the voxels by favoring detected tubular structures. Once the thresholds are visually set, various segmented volumes corresponding to the wanted artery trees were selected, hence cutting any unwanted noise that passed through both thresholds. The Frangi filter was used on different scales s ranging from 0.3 to 5. For extracting vessels there are many superior methods. However, we selected the simple filter-based approach because the next stage of this framework will run in real-time using customized TOF sequences under development in our groups.

Extraction of Skin: The skin was extracted primarily for visualization purposes, as proposed by our collaborating neurosurgeons. It generates two skins, $OBJ(3,r)$ and $OBJ(4,r)$, one from the TOF MRA and the other from the post-T1FFE, that can be used in case the patient moved during the scanning process to register the different MR data sets; this was not needed in the two studies we processed. In either data set, skin extraction entailed the following steps. First, a threshold was visually applied to the image stack, segmenting at best the whole visible skin. Then, a morphological closing was applied using a spherical mask to

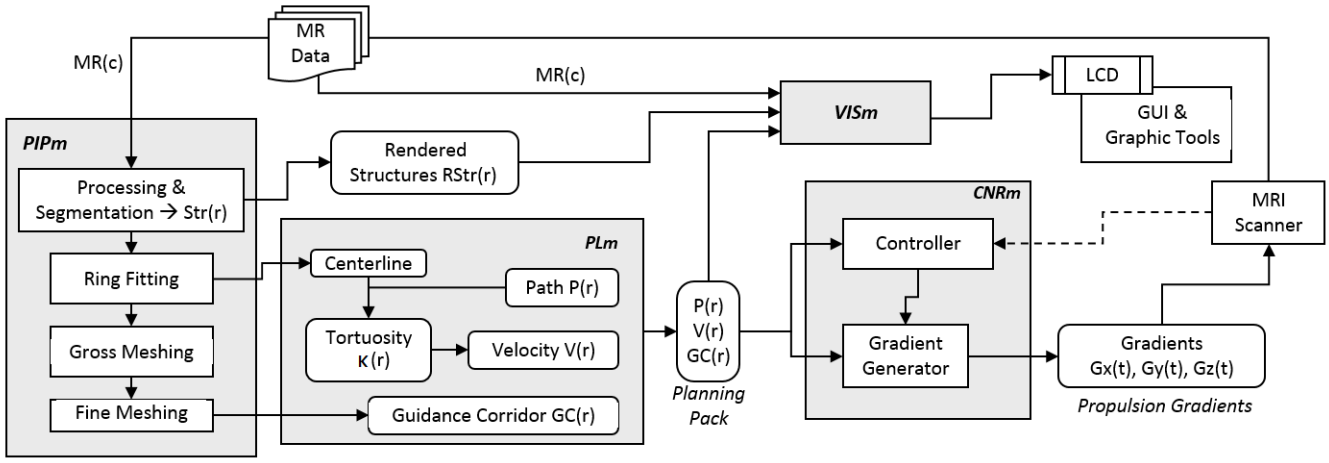

Fig. 2. Architecture of the core (refer to Table 1 for definitions) of the system depicting processes and data flow paths among them. PIPm: Preoperative Imaging Processing module; PLm: Planner module; CNRm: control module; VISm: visualization module.

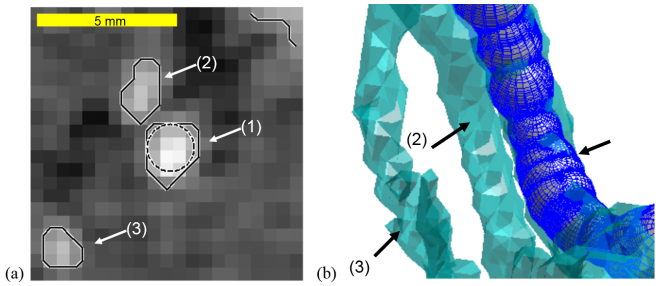

Fig. 3. Representative input and output data of the PIPm showing a zoomed in area of the original DICOM image (95th slice of the TOF-MRA set that depicts three cerebral vessels (1)-(3)). The solid line is the output of the PIPm segmentation and the dashed circle is the maximum CG circle for vessel (1). Vessel (1) reaches the lesion and the MRbot maneuvers inside this vessel. (b) Output of the PLm showing the segmented vessels and the CG mesh for vessel (1); this output is sent to the CNRm and VISm. No smoothing or interpolation was used; clearly demonstrating the challenge with native limited resolution of MR data.

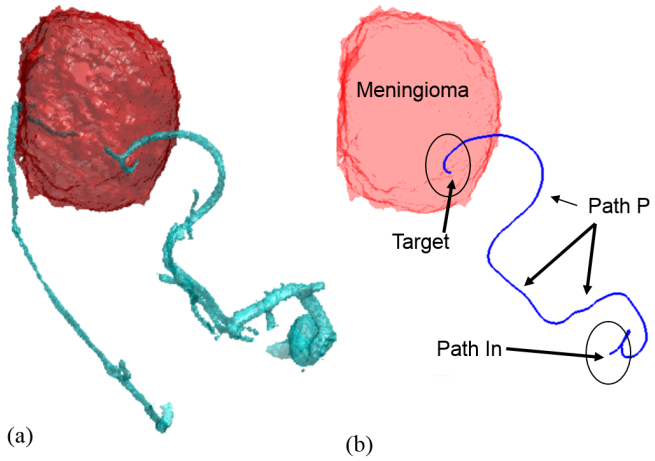

Fig. 4. (a-b) 3D scene showing (a) 3D rendered vessels and meningioma and (b) the extracted path P from the inlet to the targeted sites. All 3D structures are inherently registered and scaled to the MR scanner coordinate system. No smoothing or interpolation was used.

eliminate the segmented Rician distributed noise surrounding the skin [16]. The noise here does not need to be completely eliminated through more extensive filtering as the skin is used as a visual marker for the surgeons. Thus, the radius of the mask sphere is high enough to hide the noise. The operators have access to set the parameters in the PIPm routines, such as the thresholds in region growing and the Frangi filter.

D. Planner Module (PLm)

The input to PLm is the segmented vascular tree $OBJ(2, r)$ that is processed by the following three routines that upload their corresponding outputs to the data pipeline: (1) extraction of path $P(r)$, (2) generation of guidance corridor $GC(r)$, and (3) generation of velocity profile $V(r)$, where r is the MR coordinate system location (onto which all entities of the AoP are inherently co-registered). These tasks are: Extraction of Path $P(r)$: A first path approximation, between the inlet and the target, is generated from the previously extracted artery volumes as 26-connected graphs: each voxel is connected by two unilateral edges to its 26 neighbors. The weight of each incoming edge to the voxel v is the input to the energy function $E(v)$. The path is then the shortest one from the inlet to the target voxel, calculated using Dijkstra's algorithm. In this work, the energy function was:

$$E(v) = \exp\left\{\max_{u \in A}(d(u) - d(v))\right\}, \qquad (2)$$

where A is the set of segmented voxel in the artery tree and $d(v)$ is the distance from the voxel v to the closest voxel in the matrix not in A. This energy function was selected so the generated path approximates the center-line of the vessel and forces the shortest path through bifurcations and other imperfections along the arteries. The path generated is situated in the matrix system, which does not take into account the position of each voxel in the Reference Coordinate System (RCS). To correct this, the path is first translated into the RCS using the DICOM information present in the header

of the MRI slices: the position of each slice, and the pixel size in each slice. The same is done for a narrow band B of voxels around the set A found earlier. B is found by dilating A using a 3×3 voxel cube and then subtracting A: B is thus the first 6-connected layer of voxels surrounding A. Two voxels are 6-connected if they have at least one face in common.

Generation of Guidance Corridor(s): The path given by Dijkstra's algorithm is restricted to the voxels themselves and may thus have sharp turns or may contain saw-like parts. The first step following the RCS translation is then to smooth the path by approximating it with a high-order B-spline. Finally, the radius of the tube is the distance between the points of the B-spline and the closest point in B. The result is a set of points representing a path along with a radius value describing a corridor that can be used as a virtual fixture. This corridor can then be reduced, either using a constant safety margin, or a percentage of the initial corridor to create the safety guidance corridor ensuring that any object going through will not touch the inner walls of the vessels.

Generation of velocity profile: This routine generates a targeted velocity profile $V(r)$ along the path $P(r)$, calculating its vector for each one of the points of the path. $V(r)$ is assigned to zero at *In* and T while for any other location $V(r)$ is calculated with:

$$V(r) = \frac{V_0}{1 + \kappa(r)/\kappa_0} \cdot \frac{R_s - R_{GC}(r)}{R_0} \tag{3}$$

where R_s is the radius of the MRbot and V_0, κ_0 and R_0 are constants allowing to adjust the velocity profile.

E. Control module

The controller performs a control of the velocity $\mathbf{V}_s$ of the MRbot as well as its position $\mathbf{P}_s$. A setpoint first needs to be generated. The point of $\mathbf{P}(r)$ that is the closest to $\mathbf{P}_s$ is selected. This point (denoted $\mathbf{P}_c$) is taken as the reference point. The desired velocity at this point is $\mathbf{V}_c$. Errors on the position and velocity can be calculated with:

$$\textit{Position\_error} = |\mathbf{P}_s - \mathbf{P}_c| \tag{4}$$

$$\textit{Velocity\_error} = |\mathbf{V}_s - \mathbf{V}_c| \tag{5}$$

A block diagram of the controller is presented in Figure 5. The controller is composed of a PID regulator and a feedforward component that directly outputs the optimal control. The optimal control F_{opt} corresponds to the gradient that allows compensating for the drag produced by the blood on the sphere:

$$F_{\text{opt}} = \frac{1}{2} \cdot C_d \cdot \rho \cdot A \cdot |\mathbf{V}_{\text{blood}} - \mathbf{V}_c| \tag{6}$$

with C_d being the drag coefficient, ρ the density of blood (1025 Kg/m^3), A the reference area, and $\mathbf{V}_{\text{blood}}$ the blood velocity vector.

The PID regulator takes as input the sum of the velocity error and the position error. The position error is multiplied by a coefficient k that sets the importance of the position control with respect to the velocity control. In a practical application, the velocity can be obtained from the position measurement by using a Kalman filter.

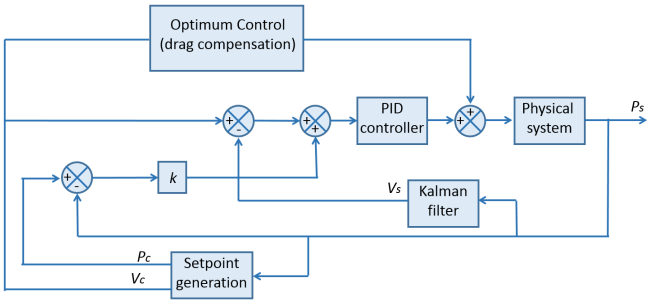

Fig. 5. Diagram presenting the architecture of the trajectory controller.

while *Procedure is ongoing* **do**
  Get $\mathbf{P}_s$ and $\mathbf{V}_s$;
  $\mathbf{P}_c = \arg\min_{\mathbf{P}} |\mathbf{P}_s - \mathbf{P}|$;
  Calculate the inputs to the PID regulator;
  Calculate the output from the PID regulator;
  Calculate the optimum control;
  Calculate and update the output of the controller;
end

Algorithm 1: Pseudocode of the trajectory controller.

F. Visualization module VISm

The purpose of the visualization module is to generate and update a virtual reality environment that simulates the Area of the Procedure (AoP). The visualization module can display any combinations of the following objects: MR images, the segmentation contours, the 3D guidance corridor GC, and when a simulation runs the sphere at its current position. All objects in the AoP are registered and scaled to the coordinate system of the MR scanner, which offers a natural space of visualizing 3D geometric structures. The update rate of the AoP is the same as that of the simulation, and if rtMRI is used to the rate of MR data collection [12], [13]. The AoP can be accessed by a HoloLens that polls the Host PC for updated versions of the virtual scene.

III. Modelization, Simulation and Results

A. Modelization of the physical system

The force applied to the ferromagnetic sphere is proportional to its magnetization (7). The magnetic field B_0 of an MRI machine is strong enough to saturate steel magnetically. The magnetization of the sphere was thus considered to be constant and equal to the maximum magnetization steel can have. The saturation flux density of 4750 steel is approximately 1.6 T which is equivalent to a magnetization M of 1.27E^6 A/m. The force vector applied on the sphere $\mathbf{F}_s$ is calculated using eq. 7, $\mathbf{G}$ being the gradient vector and *Vol* the volume of the sphere.

$$\mathbf{F}_s = \mathbf{G} \cdot M \cdot \textit{Vol} \tag{7}$$

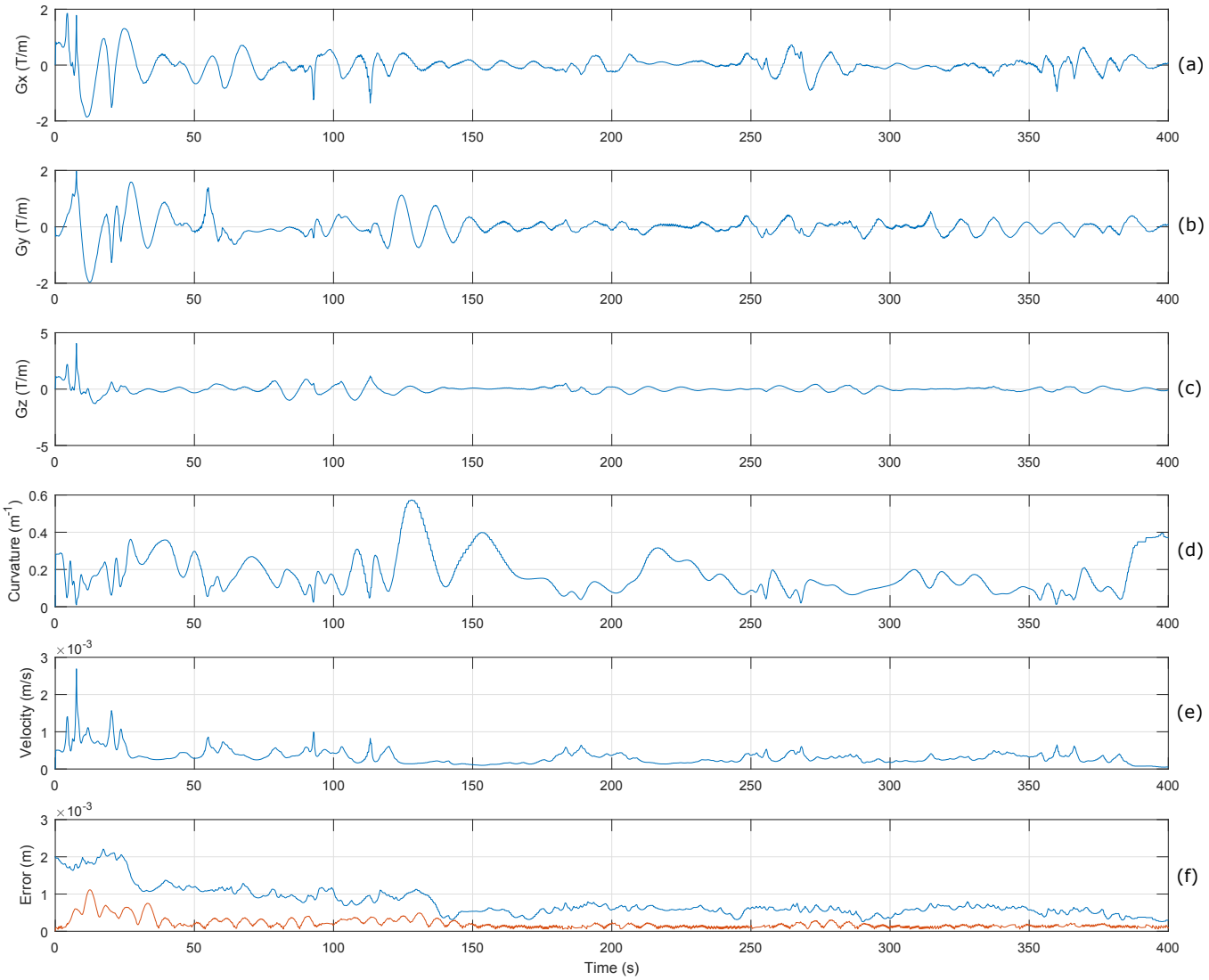

Fig. 6. Results of the simulation of the system. (a), (b) and (c) presents the gradients generated by the MRI scanner for each axis. (d) is a plot of the curvature of the path. (e) shows the velocity of the MRbot and (f) compares the positioning error (red curve) with the maximum acceptable error (blue curve). The sphere is inside the guidance corridor when the red curve is below the blue curve. The MRbot stays in the corridor during the complete navigation.

The modelization of the field produced by the MRI scanner is straightforward. MRI scanners produce almost uniform gradients inside the uniformity sphere. The gradient is therefore considered to be constant in the model.

The drag produced by the blood on the sphere was included in the model. It was assumed that the flow is separated i.e. the drag is proportional to the square of the relative speed. The drag coefficient C_d of a sphere is equal to 0.47 for a Reynolds number equal to 10^4. The drag can be calculated with (8). This equation is similar to (6) except that the velocity of the sphere $\mathbf{V}_s$ is used in place of the velocity setpoint $\mathbf{V}_c$ that was used to calculate the optimal control. It was assumed that the blood flows at a constant velocity equal to 1 mm/s and that the flow is collinear to $P(r)$.

$$F_{\text{drag}} = \frac{1}{2} \cdot C_d \cdot \rho \cdot A \cdot |\mathbf{V}_{\text{blood}} - \mathbf{V}_s| \tag{8}$$

B. Simulation Results

The model and the controller were implemented in MATLAB. Results of simulations are presented in Fig. 6 and 7. The parameters used for the PID controller are K_p=0.3, K_i=0.2 and K_d=0.01. The constant k weighting the regulation of the position is equal to 0.3. The diameter of the sphere was 0.6 mm.

As shown in Fig. 7, the sphere closely follows the planned path. It is slightly off the centerline at the beginning of navigation, where the vessel is large enough to tolerate a few millimeters of positioning error. The PLm thus automatically increased the velocity of the MRbot in this area (see Fig. 6 (e)). The curvature of the trajectory (see Fig. 6 (d)) also

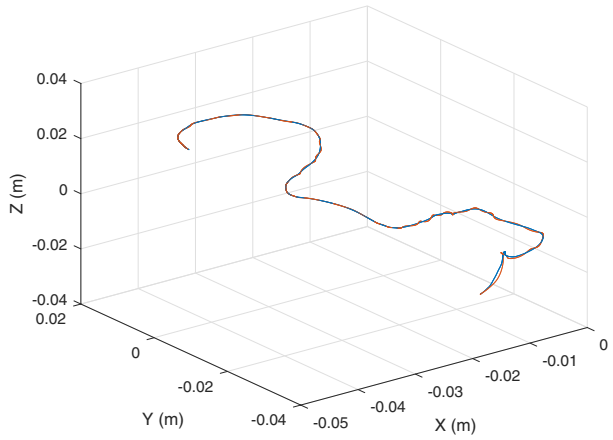

Fig. 7. 3D plot of the trajectory of the sphere. The graph shows the planed trajectory $P(r)$ (blue line) and the actual trajectory (orange line).

affects the planned velocity (see Section II-D). A plot of the error on the position of the sphere is shown in Fig. 6 (f). The maximum tolerable error corresponds to the radius of the safety corridor minus the radius of the sphere. The sphere is within the error tolerance during the complete trajectory.

To increase the tolerable error, a smaller sphere can be used. However, when the sphere becomes smaller, the gradient needs to increase to produce enough force to move the sphere. The 0.6 mm sphere in the presented simulations requires a 4.05 T/m gradient. This value is larger than the gradient produced by current commercial MRI scanners which are usually limited to values below 0.02 T/m.

IV. Discussion and Concluding Remarks

MRI actuated and guided MRbots, as carriers of therapeutic agents or even as miniature intervention effectors are a promising area in the field of interventional medicine. In addition they are an intriguing platform to develop new approaches in visual servoing, intelligent sensor control and integrating sensing and control in the same entity (the MR scanner). However, the potential impact and fate of this technology will be addressed in the field: in vivo animal studies and, eventually, human trials. Identification of meritorious clinical paradigms and appropriate evolution of this robotic technology is of paramount importance. As an alternative to catheter based interventions, maneuvering inside the cerebral vasculature to deliver an intervention is an area with potentially high merit. This work is a first step toward assessing the feasibility of such procedures and implementing a computational framework for such procedures with emphasis on how to use the pre-operative MRI data. Two primary novel features of this framework were the implementation of MRI-based virtual guidance cues and the inclusion of a trajectory-based velocity profile. The virtual guidance corridor defined a safety zone within the vessel that was then used for visual inspection and identification of areas along the path of potential safety concern (i.e. the MRbot was coming close to the vessel wall). The velocity profile used a simple approach encountered in mobile robots: the speed is reduced locally when the curvature of the path is high. This provided an additional parametric control for optimizing and modifying anatomy-based motion profiles.

The described prototype version of the computational framework was evaluated for in silico simulation of accessing a brain meningioma via the tortuous vessels of the cerebral vasculature. The velocity was adjusted during the navigation as a function of the local curvature and the radius of the guidance corridor. Therefore the PID regulator had more time to correct and stabilize the trajectory when in more tortuous segments of the vessel, ensuring that the MRbot remained within the guidance corridor.

The simulations further revealed that the procedure (i.e. MRbot dimensions and velocity profile) can be adjusted, for example, increasing velocity and/or decreasing the MRbot ferromagnetic mass require higher strength gradients to execute the maneuver. In the particular clinical paradigm, the smallest vessel was 0.7 mm diameter, and thus a 0.6 mm diameter MRbot was used. When this small entity was moved with a maximum velocity of 2.8 mm/s, the calculated control from the simulation module required a maximum gradient strength of 4 T/m. This is significantly larger than the gradient currently available in commercial MRI scanners (0.02 T/m). For this particular paradigm, possible solutions are (i) to reduce the speed of the MRbot and/or (ii) make the MRbot with higher magnetization saturation material (e.g. Holmium, rather than steel), (iii) incorporate special gradient inserts.

In this work, virtual fixtures were introduced as an approach for addressing tradeoff between temporal and spatial resolution with rtMRI for procedures that require refreshing the roadmap. This approach was further tailored primarily for sizes of MRbots that are at the scale of the narrower conduit they are asked to maneuver. The simulation model also included the drag produced by the blood on the sphere. It should be noted that this is a rather negligible contribution compared to the propulsion contribution of the flowing blood. In addition, the simulation used a rather slow blood speed of 1 mm/s; a more realistic blood flow waveform is a work in progress and will be included in a following version for this system.

The described work has certain limitations. First, the system was not connected and tested on-line with an MRI scanner. As a consequence, rtMRI was not included for MRbot tracking and on-the-fly imaging of the path forward to its motion. This is a work-in-progress based on prior works in MRbot [6], [17], [18], on-the-fly-control of the MRI scanner by the control software of a robot [19], and fast MR-sensing with modified k-space trajectories [20]. Second, the core was implemented in MATLAB for streamlining development, testing and processing the output; however, MATLAB is slow and memory-management inefficient for running such a system. Upon completion of its development, the code will be converted to C/C++, incorporating appropriate libraries (e.g. ITK/VTK/OpenGL), and optimized as we did before

with multithread implementation [8] and GPU acceleration [21]. In that previous work on dynamic VF extracted from MRI for cardiac interventions, the code for the generation of 4D guidance corridors was refreshed with a delay of less than 0.50 ms [8]. In that work it was also recognized that the bottleneck was the speed of MRI collection. We expect that, if appropriate MR pulse sequences are developed, the system can run the MRbots with virtually no latency at the computational core level. Third, the control module (CNRm) used a constant blood flow. A future version is planned to include a numerical approach in modeling flow [22]. Moreover, we selected certain algorithms for processing the preoperative data in the PIPm. Although many other algorithms exist, the particular choice of MR data algorithms do not affect this work.

As a concluding remark, we wish to underscore the challenging proposition of using MRI to guide such entities inside complex and narrow access paths. Motivated by the inherent low sensitivity of MRI modality that prevents collecting high SNR, and often high CNR, images in real-time, we describe a computational approach that uses MR-based virtual fixtures to set an access corridor that offers an operator assigned safety margin (for a more or less conservative approach) for visual servoing, image-based MRbot control, or force-feedback-assisted manual control. The next step is to develop special MR pulse sequences that will allow faster tracking of the MRbot, as well as refreshment of the path forward its motion. Only with improved real-time sensing may we claim that this robotic technology can contribute to interventional medicine.

REFERENCES

[1] Arnaud Chanu, Ouajdi Felfoul, Gilles Beaudoin, and Sylvain Martel. Adapting the clinical MRI software environment for real-time navigation of an endovascular untethered ferromagnetic bead for future endovascular interventions. *Magnetic Resonance in medicine*, 59(6):1287–1297, 2008.

[2] J-B Mathieu, Gilles Beaudoin, and Sylvain Martel. Method of propulsion of a ferromagnetic core in the cardiovascular system through magnetic gradients generated by an MRI system. *IEEE Transactions on Biomedical Engineering*, 53(2):292–299, 2006.

[3] Ouajdi Felfoul, Jean-Baptiste Mathieu, Gilles Beaudoin, and Sylvain Martel. In vivo MR-tracking based on magnetic signature selective excitation. *IEEE Transactions on Medical Imaging*, 27(1):28–35, 2008.

[4] Metin Sitti, Hakan Ceylan, Wenqi Hu, Joshua Giltinan, Mehmet Turan, Sehyuk Yim, and Eric Diller. Biomedical applications of untethered mobile milli/microrobots. *Proceedings of the IEEE*, 103(2):205–224, 2015.

[5] A. Becker and T. Bretl. Approximate steering of a unicycle under bounded model perturbation using ensemble control. *IEEE Transactions on Robotics*, 28(3):580–591, June 2012.

[6] Ouajdi Felfoul, Aaron T Becker, Georgios Fagogenis, and Pierre E Dupont. Simultaneous steering and imaging of magnetic particles using MRI toward delivery of therapeutics. *Scientific Reports*, 6, 2016.

[7] Sylvain Martel, Jean-Baptiste Mathieu, Ouajdi Felfoul, Arnaud Chanu, Eric Aboussouan, Samer Tamaz, Pierre Pouponneau, LHocine Yahia, Gilles Beaudoin, Gilles Soulez, et al. Automatic navigation of an untethered device in the artery of a living animal using a conventional clinical magnetic resonance imaging system. *Applied physics letters*, 90(11):114105, 2007.

[8] Nikhil V Navkar, Zhigang Deng, Dipan J Shah, and Nikolaos V Tsekos. A framework for integrating real-time MRI with robot control: application to simulated transapical cardiac interventions. *IEEE Transactions on Biomedical Engineering*, 60(4):1023–1033, 2013.

[9] Nikhil V Navkar, Erol Yeniaras, Dipan J Shah, Nikolaos V Tsekos, and Zhigang Deng. Generation of 4d access corridors from real-time multislice MRI for guiding transapical aortic valvuloplasties. In *International Conference on Medical Image Computing and Computer-Assisted Intervention*, pages 251–258. Springer, 2011.

[10] R. Howe S. Park and D. Torchiana. Virtual fixtures for robot-assisted minimally-invasive cardiac surgery. *Proc. Medical Image Computing and Computer-Assisted Intervention (MICCAI)*, pages 1419–1420, 2001.

[11] Jing Ren, Rajni V Patel, Kenneth A McIsaac, Gerard Guiraudon, and Terry M Peters. Dynamic 3-d virtual fixtures for minimally invasive beating heart procedures. *IEEE transactions on medical imaging*, 27(8):1061–1070, 2008.

[12] Erol Yeniaras, Nikhil V Navkar, Ahmet E Sonmez, Dipan J Shah, Zhigang Deng, and Nikolaos V Tsekos. MR-based real time path planning for cardiac operations with transapical access. In *International Conference on Medical Image Computing and Computer-Assisted Intervention*, pages 25–32. Springer, 2011.

[13] Nikhil V Navkar, Zhigang Deng, Dipan J Shah, Kostas E Bekris, and Nikolaos V Tsekos. Visual and force-feedback guidance for robot-assisted interventions in the beating heart with real-time MRI. In *Robotics and Automation (ICRA), 2012 IEEE International Conference on*, pages 689–694. IEEE, 2012.

[14] Erol Yeniaras, Nikhil Navkar, Mushabbar A Syed, and Nikolaos V Tsekos. A computational system for performing robot-assisted cardiac surgeries with MRI guidance. In *Proceedings of the 15th International Transformative Systems Conference, Dallas, USA*, pages 1–6, 2010.

[15] Regina Pohle and Klaus D Toennies. Segmentation of medical images using adaptive region growing. In *Proc. SPIE Medical Imaging*, volume 4322, pages 1337–1346, 2001.

[16] Hákon Gudbjartsson and Samuel Patz. The rician distribution of noisy MRI data. *Magnetic resonance in medicine*, 34(6):910–914, 1995.

[17] Ouajdi Felfoul, Aaron Becker, Christos Bergeles, and Pierre E Dupont. Achieving commutation control of an MRI -powered robot actuator. *IEEE Transactions on Robotics*, 31(2):387–399, 2015.

[18] Becker A. T., Felfoul O., Huang L., and Dupont P. E. MRI -powered robotics. *International Symposium on Robotics Research*, 2015.

[19] Eftychios Christoforou, Erbil Akbudak, Alpay Ozcan, Menelaos Karanikolas, and Nikolaos V Tsekos. Performance of interventions with manipulator-driven real-time mr guidance: implementation and initial in vitro tests. *Magnetic resonance imaging*, 25(1):69–77, 2007.

[20] Dawei Gui and Nikolaos V Tsekos. Dynamic imaging of contrast-enhanced coronary vessels with a magnetization prepared rotated stripe keyhole acquisition. *Journal of Magnetic Resonance Imaging*, 25(1):222–230, 2007.

[21] Mario Rincón-Nigro, Nikhil V Navkar, Nikolaos V Tsekos, and Zhigang Deng. GPU-accelerated interactive visualization and planning of neurosurgical interventions. *IEEE computer graphics and applications*, 34(1):22–31, 2014.

[22] A Salimi, J Mohammadpour, K Grigoriadis, and NV Tsekos. Dynamic simulation of blood flow effects on flexible manipulators during intracardiac procedures on the beating heart. In *ASME 2011 Dynamic Systems and Control Conference and Bath/ASME Symposium on Fluid Power and Motion Control*, pages 487–494. American Society of Mechanical Engineers, 2011.

Project: Field calculation
(id: MAGCALC)

Theme: Calculate the field produced by assemblies of solenoid coils.
Provided by Instructor: Description of the calculation method

Code specifics:
A GUI that shows Current Distributions, field, flux density and cut through projections on X, Y, Z. Graphics tool allows interactively adjusting the distribution of the currents

Input:
1. The number of solenoids, their position and orientation
2. Size of the coils Size(j)
3. Cut through Size of distribution (rectangular) LX(J), Lz(J)

Output:
1. The field H (Hx, Hy, Hz)(i) and flux density B (Bx, By, Bz)(i)
2. Isosurfaces for an operator requested B value
1. Volume (as isosurfaces) with operator requested gradient (in ppm of Bcenter)

Notes on the Modelization of the Magnetic Field

Notations: H is the magnetic field (A/m), B is the flux density (T).

1. Flux density produced by a single current loop in all space:

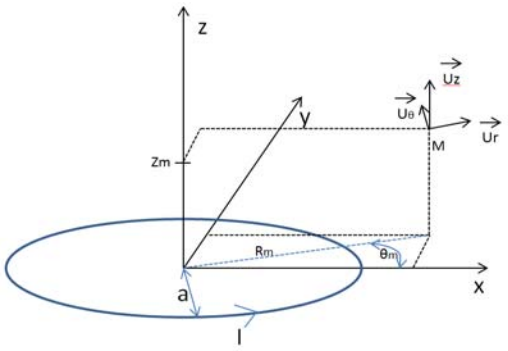

According to [1], the flux density produced by a circular current loop in all space is:

$$Bz = \frac{\mu_0 . I}{\pi . 2 . \delta^2 . \beta}[(a^2 - \rho^2 - z^2)(E(k^2)) + \delta^2 K(k^2)]$$

$$B\theta = \frac{\mu_0 . I . z}{\pi . 2 . \delta^2 . \beta . \rho}[(a^2 + \rho^2 + z^2)(E(k^2)) - \delta^2 K(k^2)]$$

$$\delta = \sqrt{a^2 + Rm^2 + Zm^2 - 2.a.Rm}$$

$$\beta = \sqrt{a^2 + Rm^2 + Zm^2 + 2.a.Rm}$$

$$k^2 = 1 - \frac{\delta^2}{\delta^2}$$

K(x) and E(x) are the complete elliptic integral of the first and second kind respectively.
[1]: **Simple Analytic Expressions for the Magnetic Field of a Circular Current Loop**, James Simpson, John Lane, Christopher Immer, and Robert Youngquist, 2001.

Matlab implementation:

This function has been implemented into matlab.

```
[ B ] = Field_single_loop( M,I,a )
```

B: returned result. Vector containing each component of the magnetic flux density in the cylindrical coordinate system [Br,Bθ,Bz], value are in Tesla.
M: Vector containing the coordinates of the calculation point in the cylindrical coordinate system. Values are in meters.
A: radius of the current loop (meters)
I: current in the loop (in amps).

Magnetic flux density produced by a single cylindrical coil in all space:

The cylindrical coil is discretized into currents loop. The magnetic field is calculated by summing the field produced by each current loop. The previous function is used to calculate the flux density produced by the current loops.

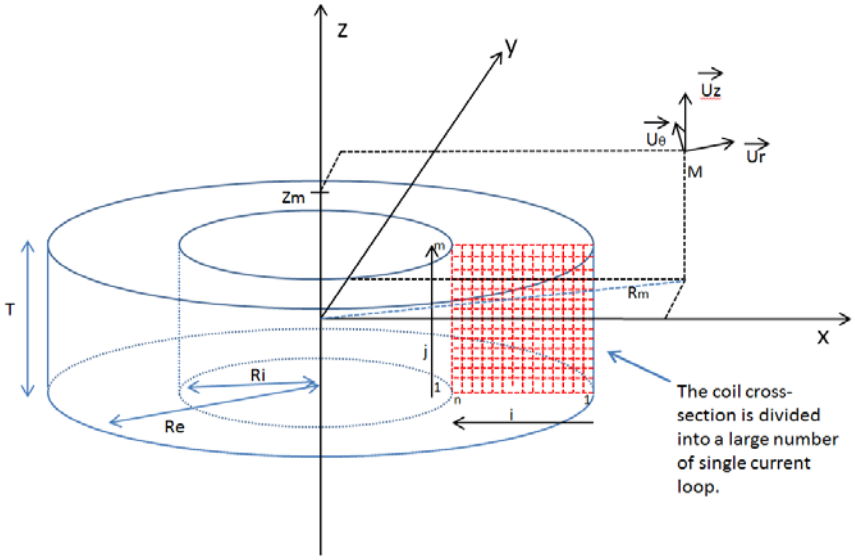

The flux density Bij produced by the current loop i,j at the calculation point M(Rm, θm, Zm) is:

$$Bij = Field_{single_{loop}([Rm,\theta m,Zm-Zj],I,ai)}$$

Where Zj is the Z coordinate of the considered current loop: $Zj = \frac{T.j}{m} - \frac{T}{2.m} - \frac{T}{2}$

And ai is the radius of the considered current loop: $ai = Ri + \frac{Re - Ri}{n}.i - \frac{Re - Ri}{2.n}$

The total flux density at the point M is the vectorial sum of the flux density produced by each current loop:

$$B = \sum_{j=1}^{m}\sum_{i=1}^{n} Field_{single_{loop}([Rm,\theta m,Zm-Zj],I,ai)}$$

Matlab implementation:

This function has been implemented into matlab:
[B] = Field_single_coil(M,Re,Ri,T,Itot)
B: returned result. Vector containing each component of the magnetic flux density in the cylindrical coordinate system [Br,Bθ,Bz], value are in Tesla.
M: Vector containing the coordinates of the calculation point in the cylindrical coordinate system. Values are in meters.
Re: External radius of the coil in meters.
Ri: Internal radius of the coil in meters.
T: thickness of the coil in meters.
Itot: Total current inside the coil, in amps. It is equal to the current in the electric wire multiplied by the number of turns.

Study the following so you see how we treat 2 solenoids; your project will be for any arbitrary number of coils

3/ Magnetic flux density produced by two cylindrical coils in all space

The field produced by two coils is calculated by summing the flux density produced by each coil. The two coils axis are collinear to the z axis of the cylindrical coordinate system. The center of the coils are separated by d.

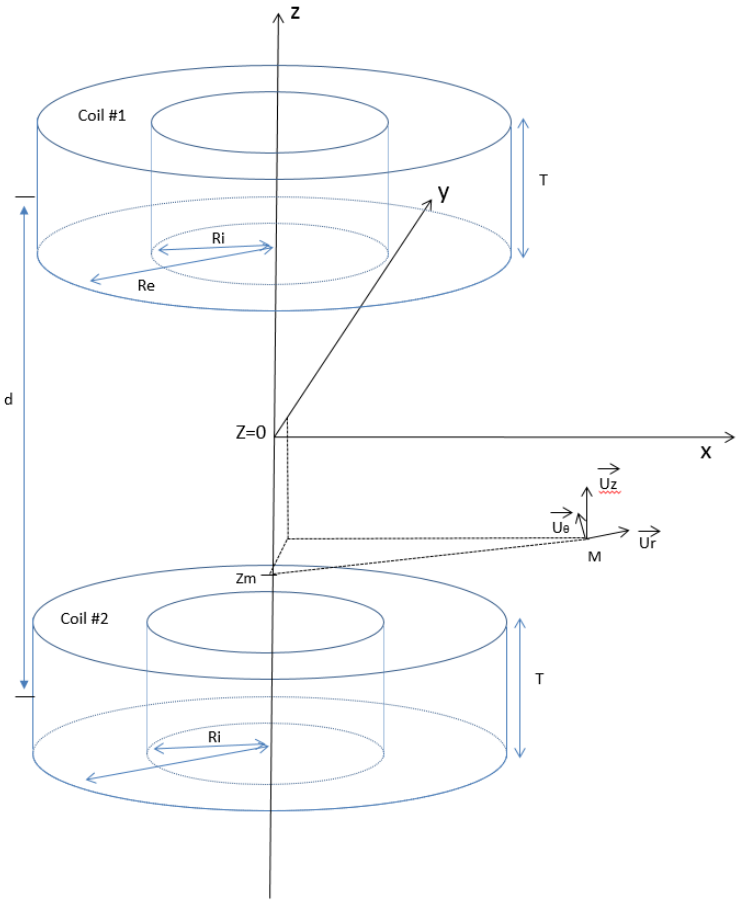

The flux density B produced by the two coils at the calculation point M(Rm, θm, Zm) is:

B = Field_single_coil($\left[Rm, \theta m, Zm - \frac{d}{2}\right]$,Re,Ri,T,Itot1)+ Field_single_coil($\left[Rm, \theta m, Zm + \frac{d}{2}\right]$,Re,Ri,T,Itot2)

Matlab Implementation

This function has been implemented into matlab.

[B] = Field_two_coils(M,Re,Ri,T,d,Itot1,Itot2)

B: returned result. Vector containing each component of the magnetic flux density in the cylindrical coordinate system [Br,Bθ,Bz], value are in Tesla.

M: Vector containing the coordinates of the calculation point in the cylindrical coordinate system. Values are in meters.

Re: External radius of the coil in meters.

Ri: Internal radius of the coil in meters.

T: thickness of the coil in meters.

d: distance between the center of the coils

Itot1: Total current inside the coil #1, in amps. It is equal to the current in the electric wire multiplied by the number of turns.

Itot2: Total current inside the coil #2, in amps. It is equal to the current in the electric wire multiplied by the number of turns.